THE EFFECT OF ANNEALING AND HEATED DEPOSITION ON ALPHA AND BETA PHASE FORMATION FOR TANTALUM THIN FILMS

by

Maxwell Keith McIntyre

B.S. in Applied Physics, Lock Haven University, 2016

Submitted to the Graduate Faculty of

Swanson School of Engineering in partial fulfillment

of the requirements for the degree of

Master of Science in Materials Science and Engineering

University of Pittsburgh

2018

UNIVERSITY OF PITTSBURGH

SWANSON SCHOOL OF ENGINEERING

This thesis was presented

by

Maxwell Keith McIntyre

It was defended on

July 19, 2018

and approved by

Markus Chmielus, PhD, Assistant Professor

Department of Mechanical Engineering and Materials Science

Ian Nettleship, PhD, Associate Professor

Department of Mechanical Engineering and Materials Science

Wissam Saidi, PhD, Associate Professor

Department of Mechanical Engineering and Materials Science

Thesis Advisor: Markus Chmielus, PhD, Assistant Professor

Department of Mechanical Engineering and Materials Science

THE EFFECT OF ANNEALING AND HEATED DEPOSITION ON ALPHA AND BETA PHASE FORMATION FOR TANTALUM THIN FILMS

Maxwell Keith McIntyre, M.S.

University of Pittsburgh, 2018

Tantalum thin films were deposited via magnetron sputtering. The phase of the deposited thin film was investigated. The tetragonal β-Ta phase possesses different properties when compared with the bcc α-Ta phase. There are applications for both phases but the mechanisms by which phases are formed is still unclear. Three categories of Ta thin film were generated then characterized: as-deposited, annealed, and heated deposition. The thermomechanical properties of Ta thin films were tested by altering deposition and post-deposition conditions and measuring stress evolution. The phase of samples was studied via resistivity measurements and offset/glancing incidence x-ray diffraction. X-ray photoelectron spectroscopy was used for elemental analysis and to confirm film thickness. It is shown that as-deposited conditions lead to β-Ta growth, while annealing to 240 ˚C causes a β to α-Ta phase transformation. The lower than previously reported phase transformation temperature is shown to be due to that lack of oxygen impurities which form TaO_2. Heated deposition at 350 °C consistently generated α-Ta while forming a Ta-Si interface region. XRD and XPS measurements confirm the presence of a $TaSi_2$ layer in annealed and heated deposition samples. These results indicate the importance of the sublayer prior to film deposition in dictating which Ta phase forms.

TABLE OF CONTENTS

LIST OF TABLES

Table **Page**

LIST OF FIGURES

Figure **Page**

ACKNOWLEDGMENTS

I would like to thank my thesis advisor Markus Chmielus Ph.D. of the Swanson School of Engineering at the University of Pittsburgh. Thank you for your guidance and assistance with this project.

I would also like to thank Jakub Toman, Amir Mostafaei, and Erica Stevens, Jakub for his contributions in the XRD studies, Amir for providing XPS results, and Erica for the SEM imaging. In addition, I would like to thank the researchers who contributed to the project before me, Eammon Hughes and Eli Sullivan.

1.0 INTRODUCTION

This section will provide a background and motivation for tantalum thin film research. The basics of physical vapor deposition and sputtering will be introduced. Followed by a description of physics behind thin film stress and particularly for Ta applications. Lastly, this studies goals and hypothesis will be stated.

1.1 BACKGROUND AND MOTIVATION

Since 1965, when a new structure of tantalum thin film was discovered, there has been research interest in reliably controlling which tantalum phase forms during thin film growth [1]. The discovery of a metastable tetragonal β phase led to an interest in producing the stable bcc α phase counterpart. Specifically, interest lies in the electrical and mechanical properties of α-Ta, as it suited the growing field of microelectronics and the need for thin film diffusion barriers [2] [3] [4] [5]. Therefore, understanding what conditions led to the formation of either phase became a research motivation. Early work focused on deposition parameters such as the working pressure, substrate temperature and material, and impurity concentration and their effects on phase formation. The phase formation was then tested with stress sensors and four-point probe resistivity [1] [6] [7]. More recent work has focused on the effects of post-deposition annealing and other characterization methods such as real-time stress measurements, x-ray diffraction (XRD) and *in-*

situ resistivity measurements to further the understanding of Ta phase transformation [8] [9] [10] [11].

The research in this thesis is motivated by furthering the understanding of Ta phase formation for thin film applications. The introduction to this thesis will present the reader with information regarding the deposition technique. The physics of thin film stress will be described in relation to the deposition technique as well as characterization instruments. Lastly, current developments in the research area of Ta thin films will be discussed. A hypothesis will be presented and then substantiated in the following sections.

1.2 SPUTTER DEPOSITION

There are two commonly used methods of individual atom transfer between a source and substrate. Chemical vapor deposition (CVD) utilizes a chemical reaction to create a vapor, while physical vapor deposition (PVD) relies on other processes such as evaporation or plasma assisted ionic bombardment. Whether physical or chemical, vapor deposition at its most fundamental is a solid substrate in contact with a vapor. The vapor deposition processes rely on vacuum chambers to control the exact composition of the vapor. A low-pressure system has a higher mean fee path between atoms. This allows source atoms a direct route to the substrate. Several variables such as the method of deposition, quality of vacuum, temperature, and substrate material influence the resulting thin film. Thermal evaporation, for example, is a PVD method. In this case, the deposition material is put in thermal contact with a heating element. Considering this method relies on temperature to evaporate the source material, the vacuum quality must be watched closely. As the

source is heated, so is the chamber. The pressure within the chamber will rise as molecules evaporate. Commonly the substrate is protected with a shutter, which is opened once the source material is evaporating. The deposition rate is represented by the number of incident atoms on the substrate, which is a function of the physical parameters of the chamber (distance and angle from source to substrate), pressure, and temperature. For evaporation, the method for creating the vapor is a thermal process. This process imparts a low amount of kinetic energy but only requires the source atoms to be present in the chamber. This why evaporation can be done in high vacuum. This leads to a slower deposition rate, but with lower defect nucleation and no damage to the substrate. This example shows how the film's composition, phase, and structure are all impacted by process variables [12] [13] [14].

Another commonly used PVD technique is sputtering. During sputter deposition, an inert, relatively high atomic mass element such as Ar is used as the sputter gas. The sputter gas, Ar, is introduced to the system to begin the deposition process. In the chamber, Ar is subjected to an electric field. This interaction will lead a plasma being formed of ionized Ar^+ atoms and free electrons. The target is negatively biased compared to the rest of the chamber and substrate. The Ar^+ ions are then accelerated towards the target. The collision releases the target material, transferring a high amount of kinetic energy. As Ar atoms are ionized, there is a cascade effect leading to more target atoms being released from the bulk. This is how a vapor of the target material is created. However, due to the presence of Ar, free electrons, and the target atoms, the operating pressure is much higher when compared to other methods. Due to these conditions, substrates are exposed to high energy electrons and target atoms that can damage the substrate. Also, Ar atoms and electrons can be sources of defects in the thin film. In an alternate process,

free electrons can also rejoin an Ar atom. The free electron's kinetic energy is transferred to a photon of the same energy [12] [14] [15].

The three most common types of sputtering are DC, RF, and magnetron. DC sputtering, also known as diode sputtering, utilizes an electric field to guide ionized sputter atoms as described previously. RF sputtering differs from DC in that it can sputter an electrically insulating target. This is possible using a blocking capacitor in conjunction with an impedance-matching network [12]. While RF sputtering improves upon DC sputtering, both suffer from slow deposition rates and possible substrate damage and defect nucleation due to uncontrolled free electrons and Ar atoms. Magnetron sputtering solves these issues by utilizing both a DC electric field and magnetic field. The DC fields purpose remains identical, while the magnetic field serves to trap free electrons in an area above the target. The electric field is set perpendicular to the target surface, allowing for the acceleration of ions into the target, while the magnetic field lines are set parallel to the target surface. Electrons trapped by the magnetic field now exist within the plasma for a longer duration. This also increases ion bombardment by concentrating the plasma directly above the target. These adjustments increase the deposition rate while protecting the substrate from damage. Without a magnet, only higher currents and pressures can achieve a higher deposition rate, but at the cost of substrate damage, more defects, and a higher concentration of impurities [14] [16] [17]. For the advantages described above, DC magnetron sputtering was used in our Ta thin film studies.

1.3 THIN FILM STRESS

Thin film stress often refers to the residual stress present after deposition. This is the case whenever a thin film bonds to a substrate or another layer of material. The residual stress-free state would exist when a layer of material is relieved of a constraint delivered by another layer or some external force. This would lead to changes in lattice parameters and curvature [12] [13].

Film stresses are commonly split into two groups: extrinsic stresses and intrinsic stresses. Extrinsic stress can be thought of as externally induced stress. These stresses are often applied after film growth and characterized by a change in the physical environment surrounding the film. Examples are temperature change affecting the coefficient of thermal expansion differences, chemical reactions, and phase transformation. Intrinsic stresses are commonly known as growth stresses. Growth stresses relate primarily to the deposition parameters and constituent materials. During deposition, the bonding between film material and substrate and the mobility of adatoms and grain boundaries effect interface stress, grain growth, and phase transformations. These are some of the factors that determine growth stress. To gain a better understanding of how stress arises in thin films and the methods by which it is measured, the next sections will discuss the physics and equations behind this subject [12] [13].

1.3.1 The Physics of Stresses

Stress is defined as the force exerted perpendicular to an area:

$$\sigma = \frac{F}{A}$$

where σ is stress over the area A and F is the force exerted on that area. With stress being equivalent to force divided by area, its units are of a pressure [N/m^2]. For the application of thin films which are commonly deposited on circular wafers, the cylindrical coordinate system is used by convention. Using this coordinate system, stress can be redefined three-dimensionally as a stress tensor:

$$\sigma_{r\theta z} = \begin{bmatrix} \frac{F_{rr}}{A_{rr}} & \frac{F_{r\theta}}{A_{r\theta}} & \frac{F_{rz}}{A_{rz}} \\ \frac{F_{\theta r}}{A_{\theta r}} & \frac{F_{\theta\theta}}{A_{\theta\theta}} & \frac{F_{\theta z}}{A_{\theta z}} \\ \frac{F_{zr}}{A_{zr}} & \frac{F_{z\theta}}{A_{z\theta}} & \frac{F_{zz}}{A_{zz}} \end{bmatrix}$$

This can be visualized in Figure 1 (Center) with a geometrical representation of the stresses principal axes in cylindrical coordinates. This representation can be thought of as an infinitesimally small portion of the thin film. In the ideal case of neglecting the external application of forces to the system of a thin film and substrate, stress can be attributed to the interaction between the film and substrate. Examining Hooke's Law in terms of stress-strain yields an equation to relates a measurable quantity, strain, to stress.

$$F = -k * \Delta x \qquad \Longrightarrow \qquad \sigma = E * \varepsilon$$

Hooke's Law originally defined the restoring force F of a spring as the product of its spring constant k and the displacement, Δx. This understanding can be extended to materials where some

factor causing force is directly proportional to displacement or material deformation. Therefore, Hooke's Law can be reinterpreted in terms of a stress component σ which causes a strain or material deformation ε, with the spring constant or elastic modulus E being a material-dependent constant. Figure 1 (Top left and right) are examples of a film and substrate experiencing compressive and tensile stresses, respectively. To understand the total effects of stress in this system, strain must be examined [12].

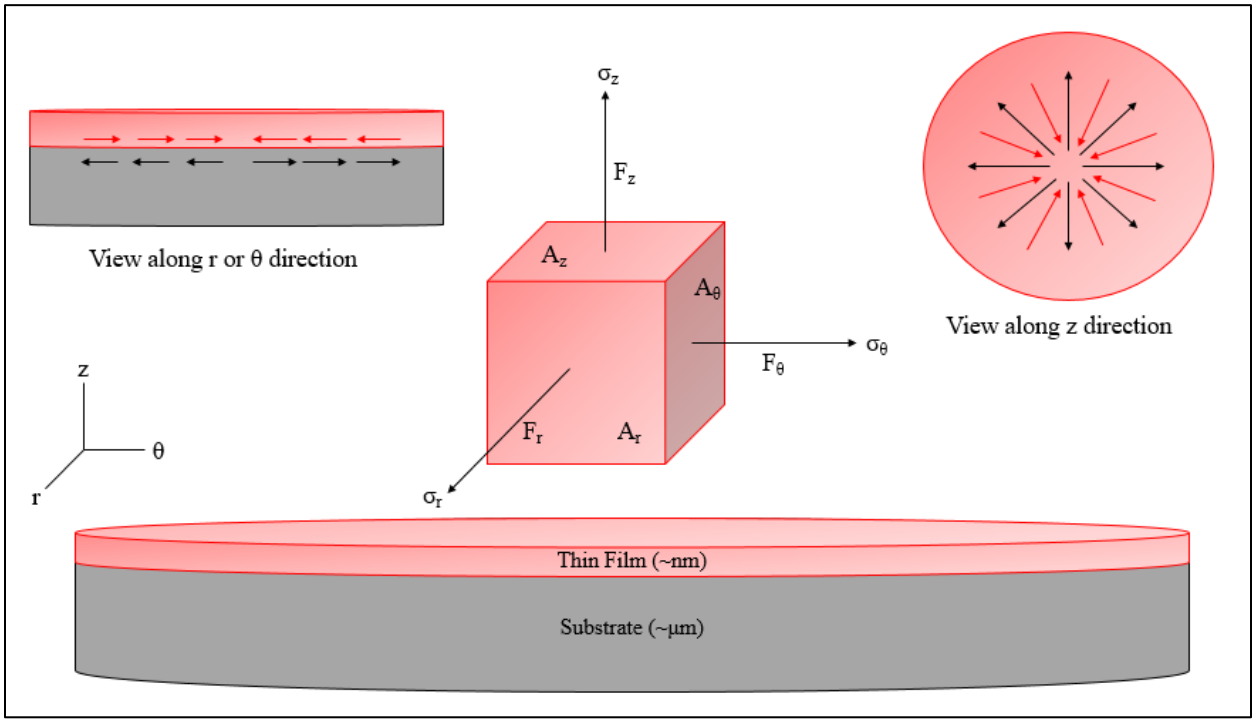

Figure 1: (Center) A geometrical representation of stress where its principal axes are in cylindrical coordinates. (Bottom) The substrate with the thin film layer, the above segment represents an infinitesimally small portion of the thin film. (Top Left) A view along the r or θ direction of the opposing stresses in the thin film and substrate. (Top Right) A view along the z-direction of the opposing stresses in the thin film and substrate.

In general, strain is a measurement of a materials deformation under a stress. For this application, the engineering or Cauchy strain will be primarily discussed. Engineering strain is defined as:

$$e = \frac{\Delta L}{L}$$

Where e is the engineering strain, ΔL is the change in length, and L is the initial length. As described previously, Hooke's Law relates stress and strain linearly, in one dimension. For thin film applications, a two-dimensional relationship can be more useful. Neglecting the out-of-plane stress, thin films can be examined from a biaxial point of view. Poisson's ratio relates a transverse strain to a longitudinal strain.

$$v = -\frac{\varepsilon_{transverse}}{\varepsilon_{longitudinal}} = -\frac{\frac{\Delta L_{transverse}}{L_{transverse}}}{\frac{\Delta L_{longitudinal}}{L_{longitudinal}}}$$

Figure 2 is a visual representation of Poisson's ratio, defining the variables for the above equation. When a material experiences a stress, the material deforms. Poisson's ratio compares the initial state to the displaced state resulting from the applied stress. To better understand the origins of stress in thin films, the next section will discuss how film growth occurs in vapor deposition [12].

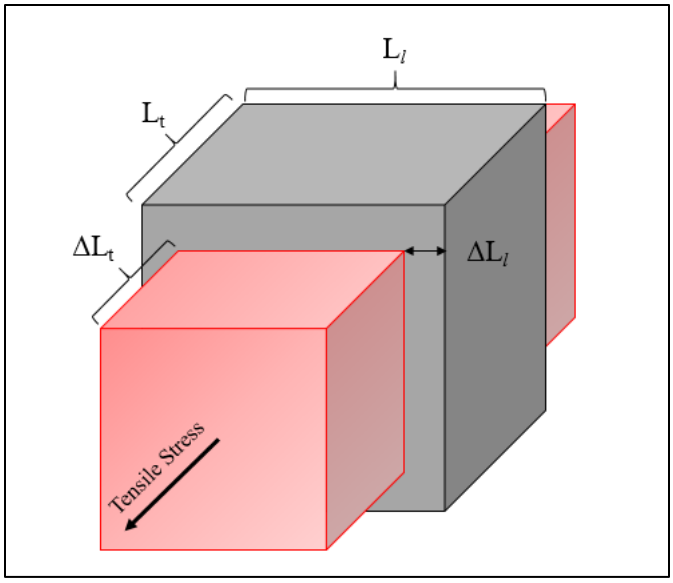

Figure 2: The original size of the material is represented by the grey cube with side lengths L_t and L_l. After a tensile stress is applied to the system, the material deforms to the red rectangular cuboid. The changes in length for the transverse and longitudinal axes divided by the original lengths provided the transverse and longitudinal strains, respectively. This is a visual representation of Poisson's ratio.

1.3.2 Thin Film Growth

Thin film growth is generally split into three modes to explain the different ways thin films are formed. Frank-van der Merve (FM) growth is a layer-by-layer growth mode where adatoms are more likely to bond with the substrate material than itself. Volmer-Weber (VW) growth is an island coalescence growth mode where adatoms favor bonding with themselves. Lastly, Stranski-Krastanov growth (SK) combines the previous modes, where initially adatoms favor the substrate then form islands. These modes are illustrated in Figure 3. To understand which modes are preferred in certain situations, the interactions between the vapor species and substrate will be discussed in more detail [12].

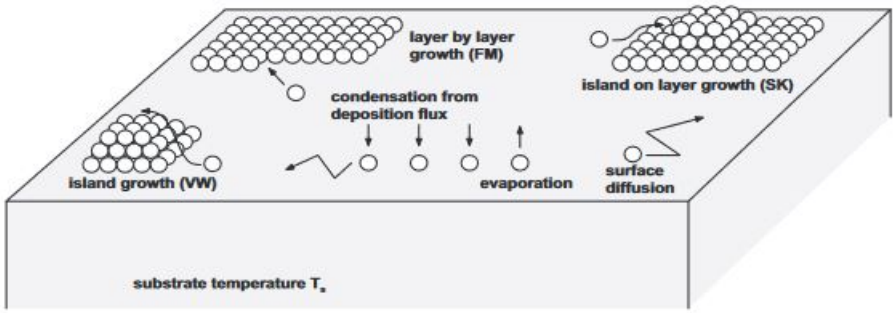

Figure 3: A schematic illustrating the ways vapor deposition can form a film on a substrate [12]. Reproduced from [https://doi.org/10.1017/CBO9780511754715], with the permission of Cambridge University Press.

In atomistic terms, the film growth begins when an atom chemically bonds to the substrate, forming an adatom. Substrate temperature and deposition rate dictate how quickly the vapor species supersaturates the substrate surface. Substrate temperature with respect to vapor material melting temperature effects the ratio of condensing atoms to evaporating atoms. Deposition rate affects the number of atoms condensing to the substrate surface. Both variables in turn affect the time an adatom has to find an equilibrium position. Low deposition rates increase the time it takes for the substrate to be supersaturated by the vapor species. High-temperature substrates increase the energy of adatoms, increasing the average length of surface diffusion. Both factors increase the time adatoms have to diffuse to equilibrium positions, favoring a single crystal film. Conversely, high deposition rates and low-temperature substrates would favor an amorphous film formation. Both factors would then limit the time an adatom has to diffuse to equilibrium positions [12] [13].

Looking at a single adatom on a substrate surface, it is positioned in an energy well. The height and location of this well are dictated by the underlying substrate or previous layer. Adatoms

can escape the energy well through thermal activation or with enough time as the probability of escape increases. These mechanisms are surface diffusion for an adatom [18].

From these concepts, the film formation mode most likely for certain scenarios can be ascertained. The previously discussed energy well can also be called a diffusion barrier. The height of this diffusion barrier, ε_d, in relation to the thermal energy present should be considered. If $\varepsilon_d >$ thermal energy, adatom mobility will be low, meaning surface diffusion is limited. This means adatoms stay bonded with the substrate where they arrive. Since this position is random and not necessarily a crystal lattice site, amorphous or polycrystalline films will grow. If $\varepsilon_d <$ thermal energy, adatom mobility will be high, meaning surface diffusion allows adatoms to reach equilibrium positions in the crystal lattice. This leads to crystalline film growth [12].

Another energy consideration is the tendency for atoms to either bond to themselves or the substrate. The variable ε_{fs} represents the tendency of atoms of the film material to bond to the substrate material. While ε_f represents to the tendency of atoms of the film material to bond to themselves. Comparing these variable's magnitude, if $\varepsilon_{fs} > \varepsilon_f$, the growth proceeds in a layer by layer fashion often referred to as the FM mode. In this mode, once adatoms are established in clusters on the substrate surface, it is energetically favorable for vapor species to attach to the edge of these clusters, where atoms can bond to the substrate. If $\varepsilon_f > \varepsilon_{fs}$, the growth proceeds through island formation then coalescence also known as mode VW mode. In this mode, once adatoms are established in clusters on the substrate surface, it is energetically favorable for the vapor species to attach to the bulk of a cluster. This forms three-dimensional islands that also grow in three dimensions until they coalesce with other islands. A third mode is a combination of the previous two, where initially planar growth is favored ($\varepsilon_{fs} > \varepsilon_f$) until a critical thickness is reached, then

island growth is favored ($\varepsilon_f > \varepsilon_{fs}$). This is SK mode where the magnitude of ε_{fs} is variable with the thickness of the film [12].

As discussed previously, sputter deposition favors the formation of polycrystalline films as crystalline and epitaxial growth require certain deposition environments and materials selection. Polycrystalline films are without a preferred texture and sputter deposition often does not seek to control crystallographic orientations. This means for most substrate and deposition material combinations; sputter deposition film growth will follow the VW mode of growth.

Figure 4 illustrates the steps in VW polycrystalline growth. The microstructure evolution begins with cluster nucleation and growth, where adatoms favor the deposition material. These islands grow until there is contact with another island where coalescence into larger islands can occur. Formation of grain boundaries also occurs at this point. This is where high deposition temperatures, various deposition rates, and post-deposition annealing can affect grain coarsening.

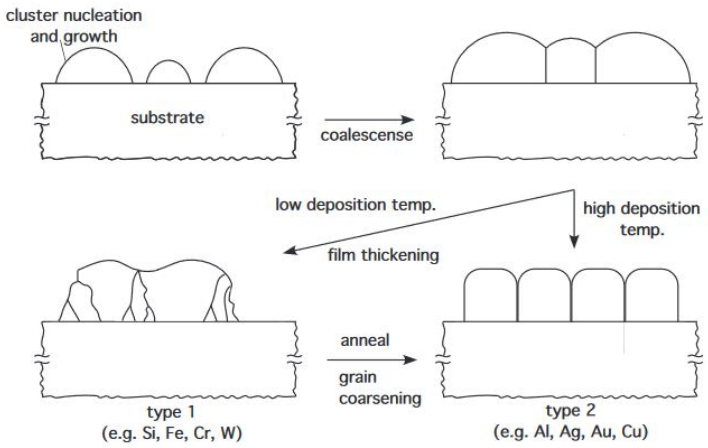

Figure 4: A diagram of the stages of film growth for a polycrystalline film. It begins with adatoms attaching to the substrate material and forming nucleation clusters. These clusters eventually coalesce, forming grain boundaries [12] [19]. Reproduced from [https://doi.org/10.1017/CBO9780511754715], with the permission of Cambridge University Press.

The growth process can be monitored *in-situ* and in real-time via a stress sensor. Since the film material adheres to the substrate material, the growth stress stemming from lattice mismatch and grain coarsening can be measured from the overall curvature of the sample. The film-substrate system will seek equilibrium via strain displacement and produce a radius of curvature. So, with careful analysis of stress evolution from a thin film deposition, the mechanisms by which the film is formed can be bettered understood. The following section will review the method by which stress measurements are possible in a sputter deposition system [12].

1.3.3 The Stoney Equation

The multi-beam optical stress sensor (MOSS) measures the curvature of a sample. This optical measurement for examining thin films has its origins in 1909, when a mechanical engineer, G. G. Stoney, was tasked to investigate the delamination and cracking of reflective films used for mirrors and searchlights. In the 1800s and early 1900s, the primary method of depositing a thin film was electrolysis or electroplating. Scientists in the 1800s had found that films were deposited under tension due to “electrostriction”. This phenomenon occurred when a metal was deposited on a thermometer and the mercury was observed to rise. Working on this basis, Stoney set out to find a relation between the deposited materials stress and the substrates observed deformation [20].

Stoney used a steel ruler, 102 mm x 12 mm x 0.32 mm, as a substrate. It was dipped into an ammonium-sulfate bath and nickel was electrolytically deposited in thicknesses from 5.6 to 46.2 μm. Stoney measured film thickness by weighing each sample pre- and post-deposition.

Deformation of the steel ruler was measured as the radius of curvature. A calibrated eyepiece in combination with a microscope measured the sagitta of the arc made by the bent ruler. Based on the amount of bending and the thickness of the film, Stoney could derive the Stoney equation.

$$\sigma_f = \frac{E_s d_s^2}{6 d_f} \rho$$

Where σ_f is the stress experienced by the film, E_s is the elastic modulus of the substrate, d_s is the substrate thickness, d_f is the film thickness, and ρ is the radius of curvature [21]. Several assumptions were made when deriving this equation and are important to consider when reapplying it. Stoney assumed that the elastic moduli of steel and nickel are roughly equivalent. In most applications this assumption can hold, modifications to the Stoney equation have added a term with Poisson's ratio for added physical property accuracy. Film thickness and radius of curvature uniformity were assumed. Film thickness must be less than substrate thickness which must be far less than the radius of curvature. Lastly, the film stress states along with the substrate curvature were assumed to be in-plane isotropic or equiaxial. Over the following century, Stoney's equation has been modified to fit certain fabrication systems, characterization tools, and material systems. In particular, the Stoney equation is the underlying principle for the MOSS technique.

With the use of the Stoney equation, the MOSS only needs to measure substrate curvature for the user to be able to calculate stress. Figure 5 is a schematic of the multi-beam optical stress sensor. The design begins with a HeNe laser that is directed at an objective lens which focuses the beam. Next, there is an etalon, a device with a pair of parallel reflective plates, that internally reflect the beam, generating an array of parallel beams. A second etalon follows that is rotated 90°, generating a 2-dimensional array of beams. The array of beams then reflects off the sample and

directly into a charge-coupled device (CCD) camera. The camera monitors the entire array simultaneously, effectively mapping a two-dimensional grid of reflected spots [20].

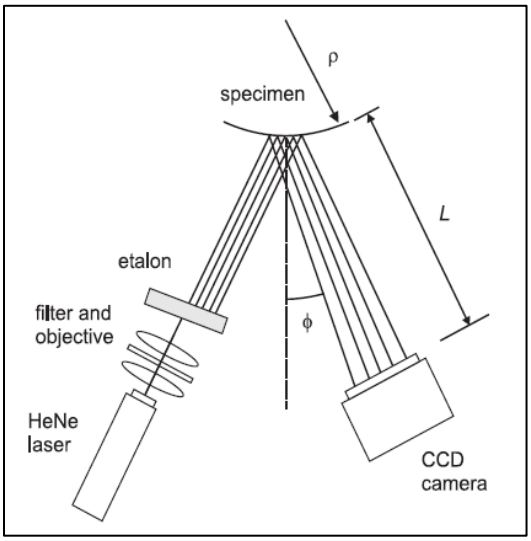

Figure 5: Schematic of the multi-beam optical stress sensor [12]. Reproduced from [https://doi.org/10.1017/CBO9780511754715], with the permission of Cambridge University Press.

From Figure 5, the angle ϕ is defined as the angle between the sample normal and the reflected beams, L is the distance from the sample to the camera, and ρ is the sample's radius of curvature. From the schematic, the following equation can be derived.

$$\kappa = \frac{1}{\rho} = \frac{\cos\phi}{2L}\left(1 - \left(\frac{D}{D_0}\right)\right)$$

Where D is defined as the average spacing between reflected beams and D_0 is the average initial spacing. From this substrate curvature value, the film stress can be calculated using the Stoney equation. Thanks to the high resolution of the CCD camera, the resolution of the MOSS is approximately a radius of curvature of 15 km. MOSS is operated continuously, with the CCD camera recording the beam spacing. This means stress evolution can be recorded, providing a

complete progression of film stress during deposition or annealing. This method also is unaffected by system vibrations because the array of beams are deflected in unison and compared back to the initial average spacing [12].

1.4 TANTALUM THIN FILMS

α-Ta is commonly seen in bulk and thin film Ta, while β-Ta forms exclusively in thin films [1] [22] [23] [24]. The stable α phase of tantalum is commonly used in tantalum electrolytic capacitors utilizing Ta's natural tendency to form a dielectric oxide layer which makes high capacitance possible due to the small volume [2]. Protective coatings are another application for α-Ta. Unlike α-Ta having low resistivity, ductility, and chemical inertness, β -Ta does not see much use due to it being brittle, reactive, and highly resistive, making it unsuitable for typical Ta applications [7] [25] [26]. In general, research surrounding metastable β-Ta has been focused on consistently achieving thin film α-Ta. Typically, Ta thin films are sputtered, yet there is no consensus on what sputter conditions consistently generate α or β-Ta. Phase formation control is undoubtedly tied to the deposition environment, therefore more research must be done investigating this area.

In recent years, there has been a resurgence in interest regarding phase formation control of Ta thin films with the discovery of a giant spin Hall effect (GSHE) in β-Ta [27]. Liu et al. have proposed that GSHE can be a source of spin current for spintronic devices. Conventional magnetoresistive random access memory (MRAM) technologies utilize electronic current flowing through a ferromagnetic thin film to generate spin currents. Spin currents apply a torque to the magnetic moment of the ferromagnet, enabling transfer of spin angular momentum. The spin

current required for the spin torque transfer is orders of magnetic lower than the conventional magnetic field induced current. This development fixes problems with larger currents writing adjacent cells or damaging barriers. β-Ta via the GSHE can improve reliability and lower the spin current in MRAM technologies making understanding phase formation for Ta thin films more significant [27].

With Ta thin films being deposited primarily by sputtering, there are several deposition conditions that can be examined in connection with phase formation. Based on previous studies several important factors arise, such as: substrate material and structure [2] [28] [29] [30], impurities on substrate and in sputter gas [9] [31] [32] [33], the energy of atoms in the plasma [8] [34] [35] [36] [37] [38] [39], and substrate temperature [6] [12] [40] [41] [42]. The two variables in these studies that this research will focus on are the impurities present in the deposition chamber and on the substrate surface and the substrate and phase transformation temperature.

The particular impurity of interest is oxygen which readily reacts with both Si and Ta forming SiO_2 and TaO_2, respectively. Other studies have detailed the effects of oxygen impurities and TaO_2 layers have on phase formation, showing it promotes β-Ta in subsequent layers [43] [44] [45] [46]. Oxygen impurities also affect the β to α phase transformation temperature. Knepper et al. studied this relationship, providing evidence that oxygen exposure and incorporation delay the transformation to higher temperatures [44].

Increasing substrate temperature has been shown to produce α-Ta with some reliability. Several studies examined substrate temperature, finding that a pre-heated substrate of ~250 $^{\circ}$C promoted α-Ta growth, citing absorbed water as a source of oxygen [28] [32] [31]. Schwartz et al. in a similar study found a heated substrate of ~800 $^{\circ}$C guaranteed α-Ta growth [6]. Other studies annealed the Ta thin films after deposition, reporting phase transformation temperatures as low as

350 °C [44] and as high as 750 °C [7]. The consensus from many thermal studies regarding Ta phase control has resulted in a wide range of reported temperatures promoting α-Ta growth. Since there is such a wide range of reported phase transformation temperatures, this variable was investigated while holding all other significant variables constant and minimizing impurities.

1.5 RESEARCH GOALS AND HYPOTHESIS

This thesis presents a method of controlling α-Ta phase formation for thin films deposited via DC magnetron sputtering. The thin films were deposited with UHV DC magnetron sputtering system which has been designed to benefit the research goals presented. The method presented has been examined with characterization instruments like MOSS sensor evolution, XRD, XPS, and four-point probe resistivity.

The first hypothesis of this research is that a β to α Ta phase transformation temperature of 240 °C was achieved because of a low amount of oxygen impurities in the deposition chamber and on the substrate. To investigate this statement, the following research goals were established:

- Develop a deposition chamber where the sample can reach temperatures in a range of 300-800 °C,
- Ensure a clean, UHV deposition environment, free of primarily oxygen and organic contamination,
- Deposit Ta thin films then anneal while observing stress evolution,
- Identify α or β phase formation in the Ta thin films and the underlying mechanisms that govern which phase forms.

The second hypothesis of this research is that pre-heating the substrate improves gas and substrate surface purity, heating during deposition improves surface diffusion, both factors promote pure α-Ta formation. To investigate this statement, the following research goals were established:

- Deposit and process Ta thin films under certain conditions: as-deposited, annealed, and heated deposition while observing stress evolution,
- Determine film thickness and elemental composition throughout the films using XPS.

2.0 EXPERIMENTAL

In this section, the system preparation and calibration, simulation, sputter deposition, and characterization steps are described in detail.

2.1 UHV SPUTTERING SYSTEM

The lab uses an ATC Orion Sputtering System for AJA International Inc (Figure 6a). The system features up to 4 magnetron sputtering sources as well as ultra-high vacuum (UHV) capabilities. This is accomplished with a combination roughing, turbo, and cryogenic pump. The pressure in the main chamber is monitored with 2 ion gauges plus a capacitance manometer. These in conjunction provide accurate readings from atmosphere to UHV. Additionally, the load lock is equipped with 2 wide range pressure gauges. Figure 6b is a rough schematic of our system with the key external components. This shows the position of the substrate in relation to the sputter sources. The substrate is attached a substrate holder that locks with a rotating column. This holder hangs directly underneath 2 quartz crystal heating lamps capable of heating the substrate to ~900 $^{\circ}$C. At the base of the main chamber, multiple magnetron sputter sources are mounted within cathode shielding and covered with a shutter. A mass flow control (MFC) connects several gases to the system, such as O_2, N_2, and Ar. Additionally, a residual gas analyzer (RGA) and multi-beam optical stress sensor (MOSS) are attached.

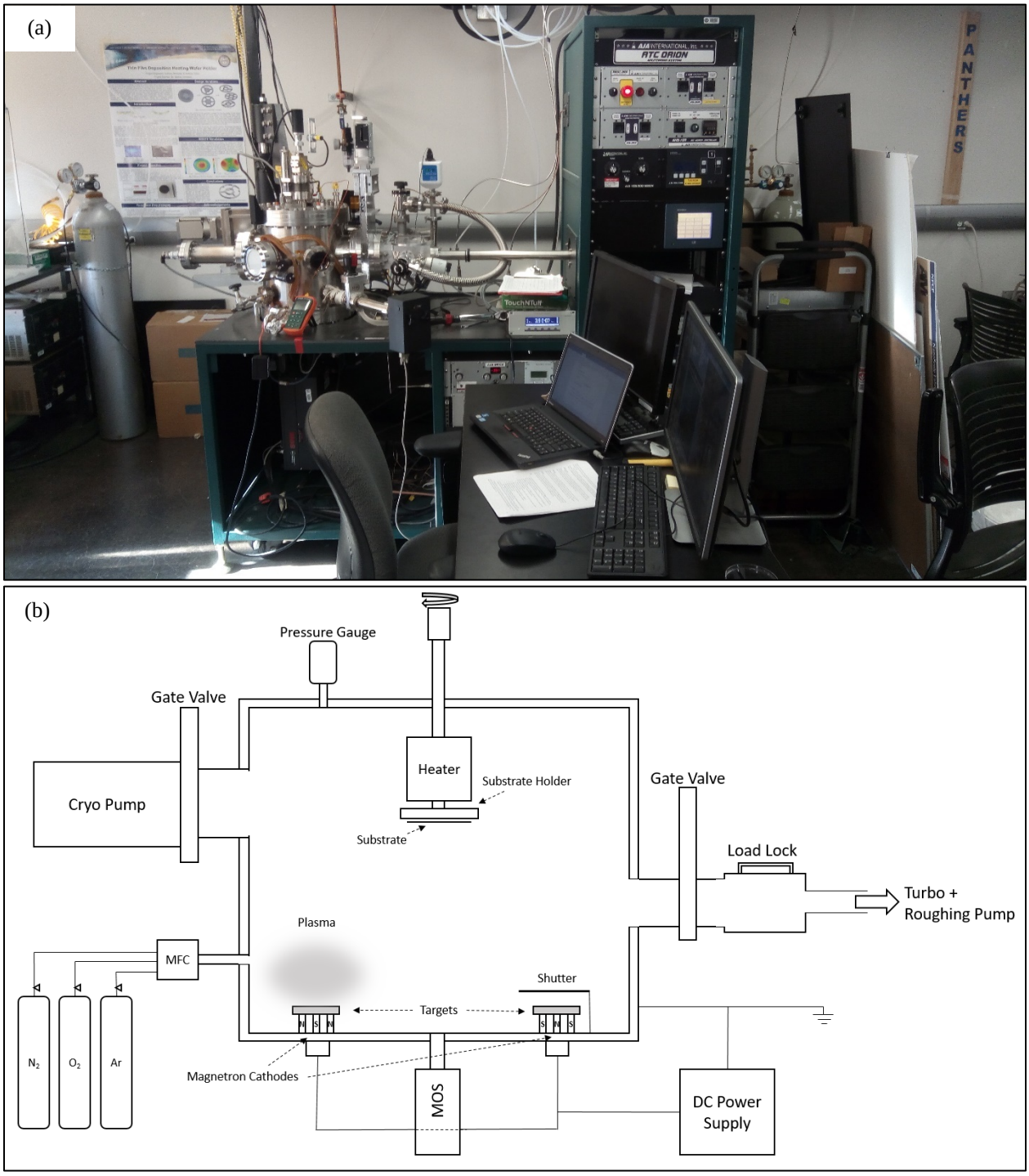

Figure 6: (a) The ATC Orion Sputtering System. (b) A schematic of our sputtering system's setup. This is not a complete schematic, it simply shows the key external technology and how it connects to the main chamber.

2.2 RESIDUAL GAS ANALYZER

The residual gas analyzer (RGA) from Extorr is attached directly to the UHV systems main chamber. An RGA is designed to analyze gas in a vacuum system via a quadrupole that senses the weight of an atom. Extorr's RGA utilizes Faraday ion detection as well as an electron multiplier to achieve a wide range of detectable gas partial pressures, from 10^{-4} to 10^{-14} Torr. Additionally, the RGA is outfitted with a compact communications and control unit (CCU) that allows for real-time control and analysis from a PC [47]. In our application, the RGA was primarily used to detect trace amounts of impurities, the results inform us about what cleaning process should be performed such as externally heating the system or running the getter pump. It was also used for the occasional helium leak check where the real-time analysis is useful for leak location detection.

Following several months with the main chamber at atmospheric pressure, it was pumped down to ~$1x10^{-6}$ Torr. The RGA was then run at room temperature. There were no bakeouts or additional pumps used aside from the turbo and roughing pumps. Figure 7 is a graph of the resulting RGA mass sweep with pressure (Torr) vs. mass (amu). The 18 amu peak corresponds with a water molecule's atomic mass. This is expected as water had undoubtedly condensed on all surfaces exposed to the atmosphere. Peaks at 1, 2, 3, 16, and 17 amu all correspond to fragments of the water parent ion. It is important to note the absence of any hydrocarbons that would be repeated across this sweep. Hydrocarbons are impurities related to pump oil, grease, and organic solvents, all being difficult to remove from a vacuum system.

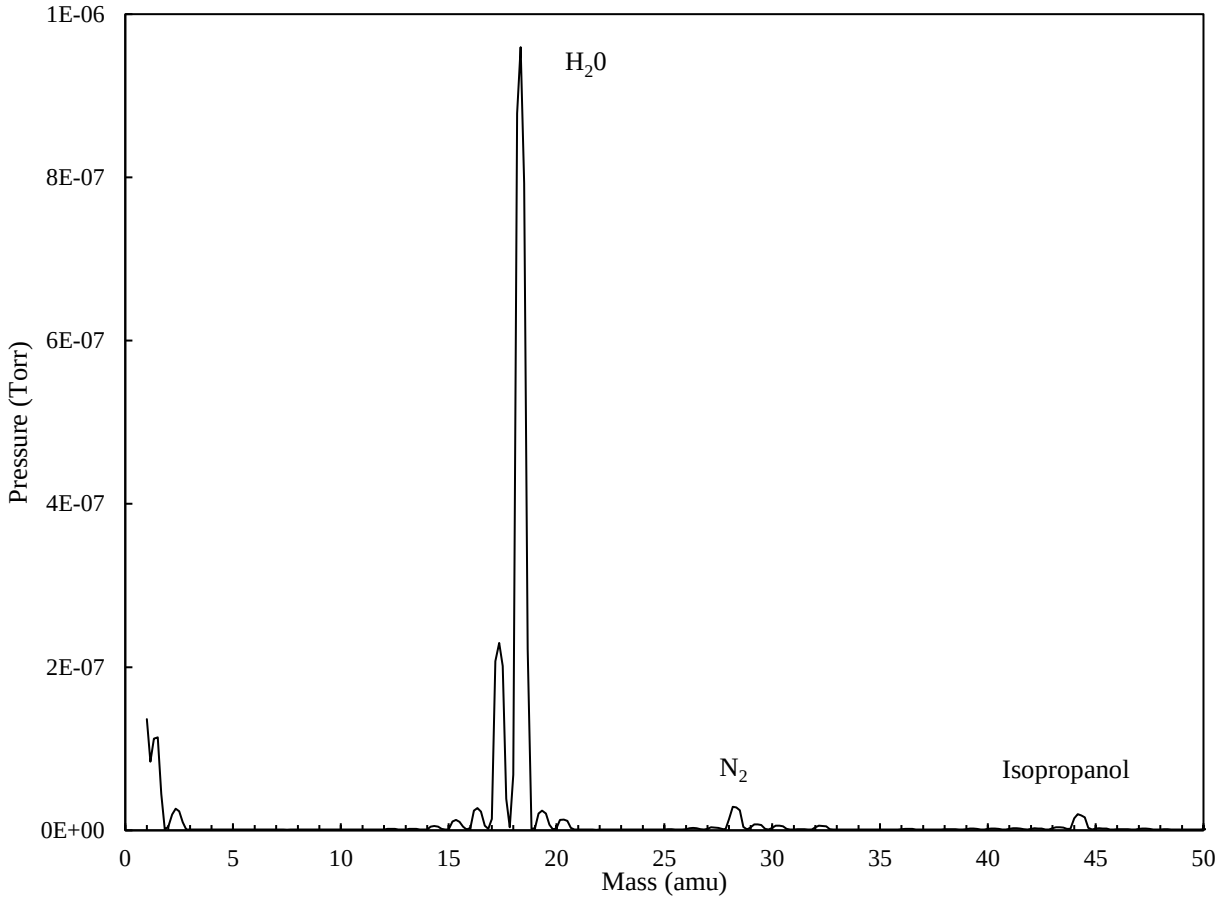

Figure 7: A RGA mass sweep with pressure (Torr) vs. mass (amu). The sweep was performed at ~1x10^{-6} Torr at room temperature. The sweep was performed after several months with the main chamber at atmosphere.

With the presence of a strong peak attributed to water molecules, additional steps were taken to remove contaminants. Many contaminants outgassed from the chamber walls for long periods of time. To accelerate this process, heating tape was applied externally to the chamber walls. By wrapping the tape around the chamber and covering it with aluminum foil, the chamber walls can be heated up to about 100°C. Additionally, a getter pump was used. A getter pump has getter material coated on it, that becomes activated when heated. Activated getter material chemically reacts with contaminant molecules in the vacuum chamber. This reaction results in the

contaminant being absorbed into the bulk of the getter material. Following these decontamination steps, the RGA was run again. Looking at Figure 8, the similar peaks appear, but at a lower partial pressure. This is most evident for the 18 amu peak or the water molecule. In Figure 7, the peak partial pressure for 18 amu is nearly $1x10^{-6}$ Torr. After heating and using the getter pump, this peak has diminished to ~$2x10^{-8}$ Torr, almost a decrease in two orders of magnitude. Successfully decontaminating the chamber leads to higher purity sputter gas and deposition [48].

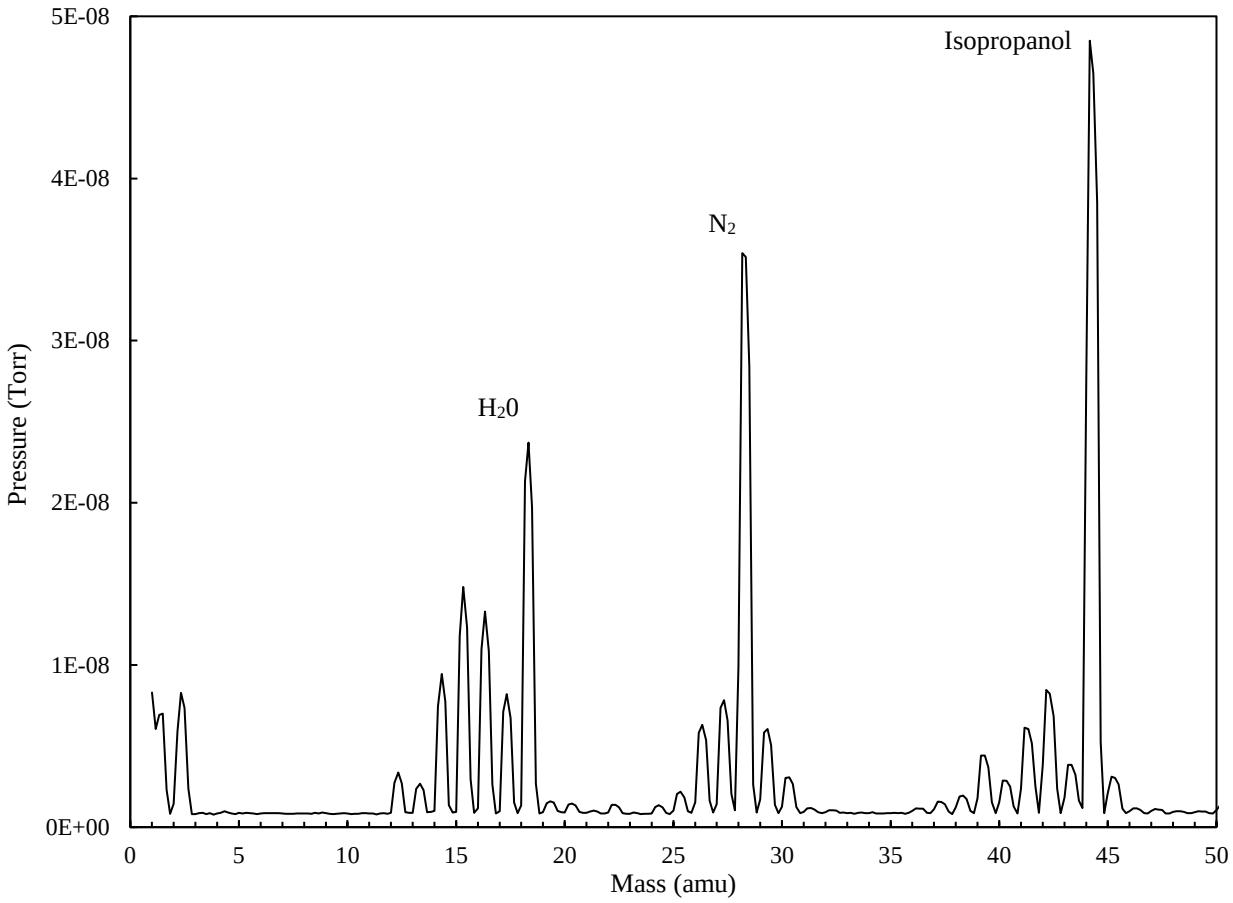

Figure 8: A RGA mass sweep with pressure (Torr) vs. mass (amu). The sweep was performed at ~$2x10^{-8}$ Torr at room temperature. The sweep was performed after the getter pump and external heating tape was used.

2.3 THERMAL CALIBRATION – ORIGINAL SUBSTRATE HOLDER

The ATC Orion Sputtering System used to deposit thin films utilizes two quartz heating lamps to provide substrate heating. They are located directly above the substrate holder. A piece of glass and ~1 mm of vacuum separates the lamps and the holder. Through the center of the two lamps is the rotating column which the holder attaches to via the three-pronged locking mechanism. Embedded in the glass, next to the rotating column is a thermocouple. This thermocouple communicates with the external heater controller. Each of these components can be seen in Figure 9c. The originally intended use of this system's setup necessitated thermal contact between the substrate and the holder (Figure 9d). The holder is made of Inconel 625, a nickel-based superalloy with notable high-temperature strength. Being ¼" thick and 3.5" in diameter, the holder has six screws that tighten to hold a 3" wafer in place. The heater could then radiate the back of the holder, which in turn would transfer the heat via conduction to the wafer. The manufacturers provided a conversion curve (Figure 10) that shows the temperature offset between the thermocouple reading and the actual sample temperature.

The primary goal of this study was to investigate the stresses in the thin film during deposition while being heated. Because of how the stress evolution measurements are taken, the substrate cannot be tightened into thermal contact with the holder, thus constraining the substrate. The substrate must have the freedom to curve in that direction. The pop out in Figure 9b shows the holder's screws not tightened, allowing the substrate to rest on the screw flaps. This provided a 1 mm gap between substrate and holder. The side effect is the lack of thermal contact between the two pieces, making the temperature offset chart no longer valid for our experimental setup.

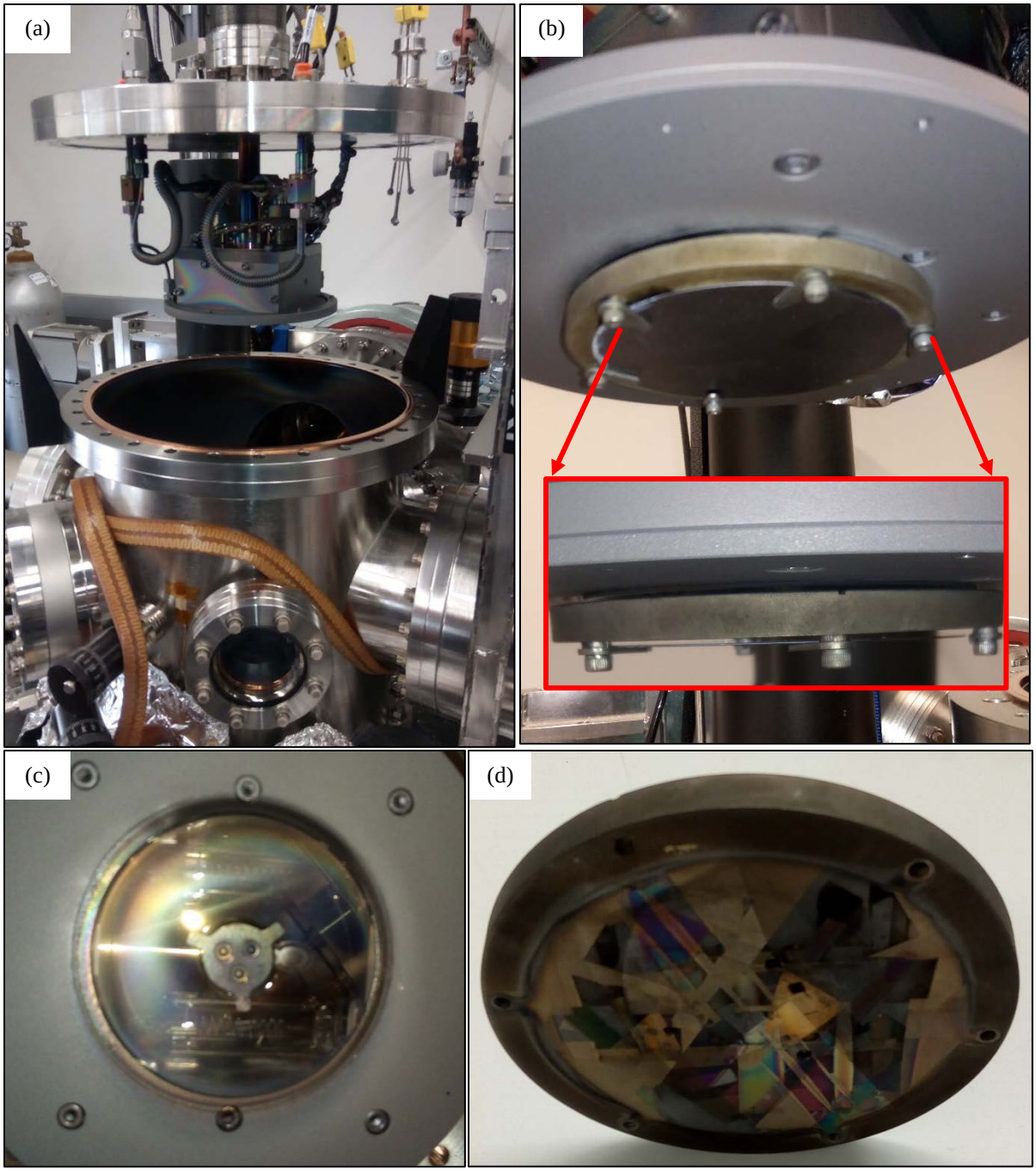

Figure 9: (a) Overview of the ATC Orion Sputtering System UHV chamber at atmospheric pressure. (b) A view of the substrate holder and wafer in place beneath the heater. (A side view of the wafers separation from the holder) (c) An upshot of the central column where the rotating column, heater, and thermocouple are located. (d) The original Inconel 625 substrate holder.

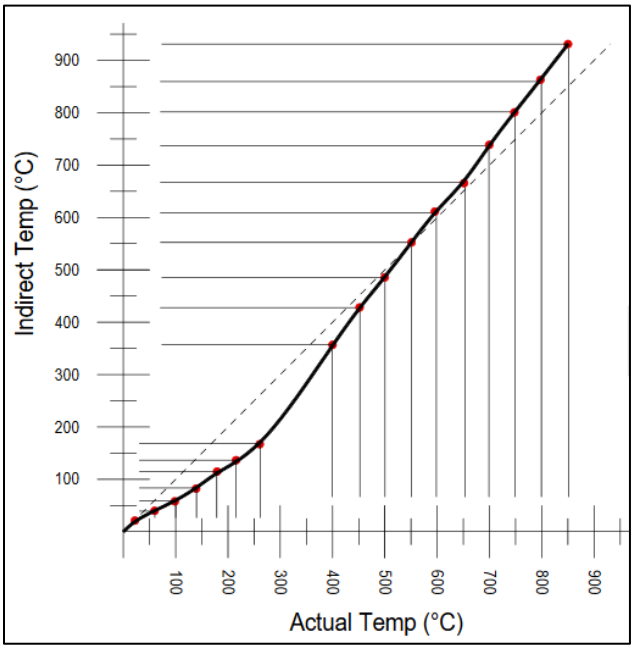

Figure 10: Temperature conversion curve provided by AJA Int. Inc. that relates the indirect temperature (thermocouple) to the actual temperature (sample).

A new temperature calibration chart was to be created by applying two additional thermocouples to the surface of the substrate (Figure 11a). Using a thermocouple feedthrough installed on the main chamber, the thermocouples were wired to an external thermometer datalogger. The datalogger communicated via a USB port to a PC, logging the actual temperature of the substrates surfaces (Figure 11b).

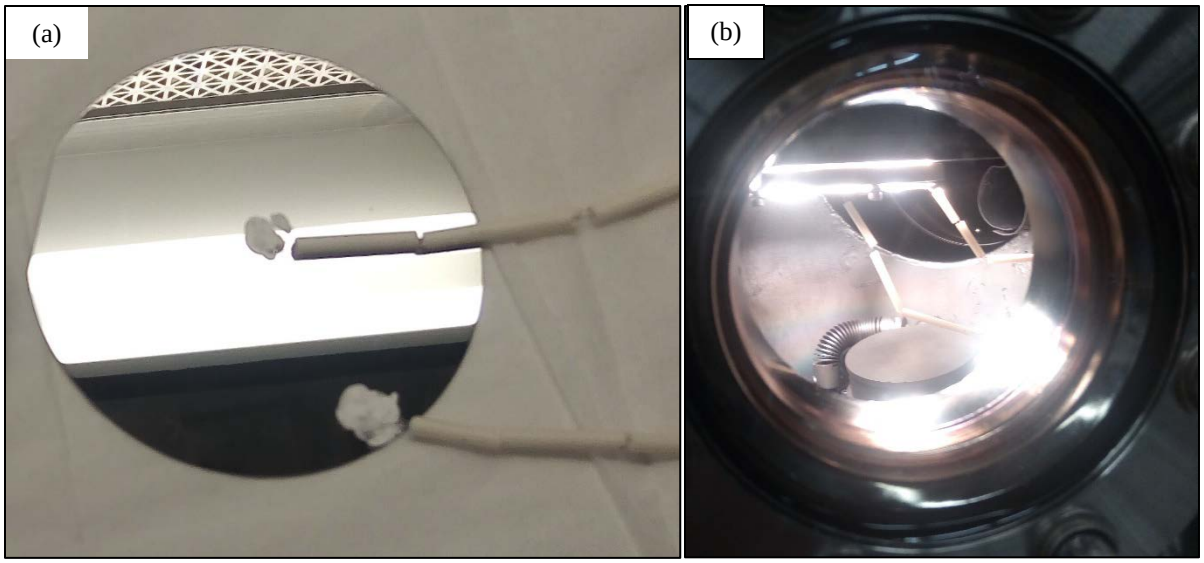

Figure 11: (a) Two thermocouples applied with high-temperature resistant ceramic adhesive to the surface of a Si wafer with a Ta thin film already deposited. (b) The substrate set in the holder inside the UHV main chamber. The quartz lamps are turned on, heating the substrate.

The sputter system's proportional-integrative-derivative (PID) heater controller was used in setpoint mode. Figure 12 is a temperature versus time graph with two series, the heater controller setpoint and the actual wafer temperature measured by the additional thermocouple. As seen in Figure 12, setpoint mode required manually setting temperature setpoints into the controller. The time at which this was performed was based on when the actual wafer temperature had plateaued. An analysis of the data shows that the actual wafer temperature never exceeded half of the setpoint. By the 500°C setpoint, the actual wafer temperature had reached 200°C. The maximum temperature capability of the system is 900°C, with an advisory not to exceed 800°C often. Based on the knowledge that tantalum phase transformation occurs in a wide but high temperature from 350-850°C, the current experimental setup was not sufficient. Therefore, modifying the existing

substrate holder to maximize heat transfer from the quartz lamps to the wafer became the primary objective.

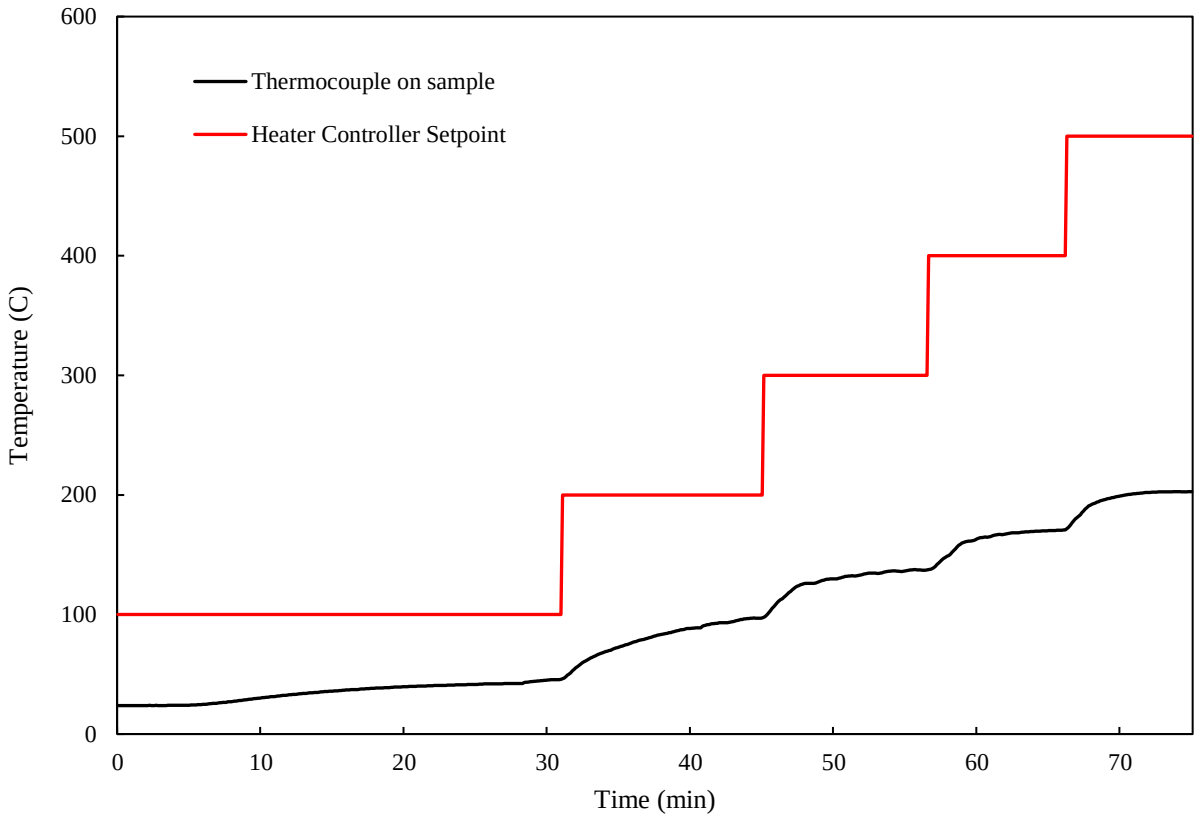

Figure 12: A thermal calibration data collection of temperature vs. time comparing the setpoint value from the heater controller to the actual temperature at the center of the wafer, read by a thermocouple.

2.4 ANSYS THERMAL SIMULATION AND ENGINEERING A NEW HOLDER

As part of a senior design project, a new substrate holder was commissioned. The objective of this project was to improve the heat transfer from the quartz lamps to the substrate. A target substrate temperature was set at 300 ˚C or greater to hopefully allow us to thermally induce a tantalum phase transformation. To do so, heat transfer via radiation must be maximized. Convective heat transfer is non-existent in vacuum and conduction is very limited due to stress experiment constraints. Figure 13 (a) is a SolidWorks rendering of the original holder design including the locking mechanism which attaches to the UHV systems rotation column. The original design was intended to have to Inconel holder absorb the radiation from the lamps and conduct it to the substrate, which was in thermal contact. However, without being in thermal contact the wafer was limited in the amount of energy it was receiving. Therefore, the new substrate holder design as seen in Figure 13 (b) was proposed to improve radiative heat transfer from the lamps to wafer.

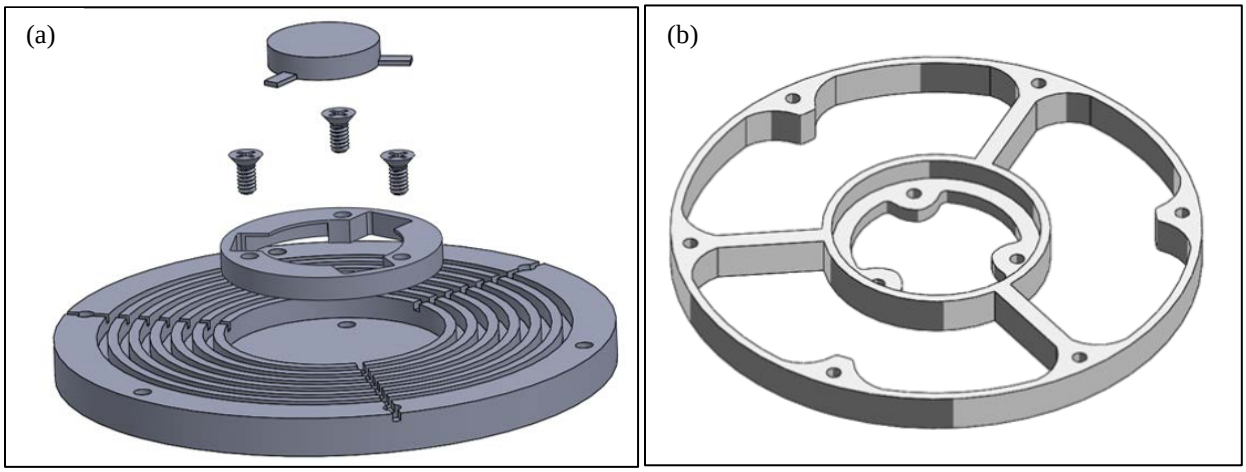

Figure 13: (a) The original substrate holder design, including the locking mechanism for load lock transfers. (b) The new substrate holder design, incorporating the previous locking mechanism.

The new holder design matched the previous in most of its physical parameters. For simplicity sake, the same locking mechanisms were utilized along with the same screw flaps to hold the wafer. Figure 14 is a SolidWorks engineering data schematic that was transferred to ANSYS and later to the 3D printer.

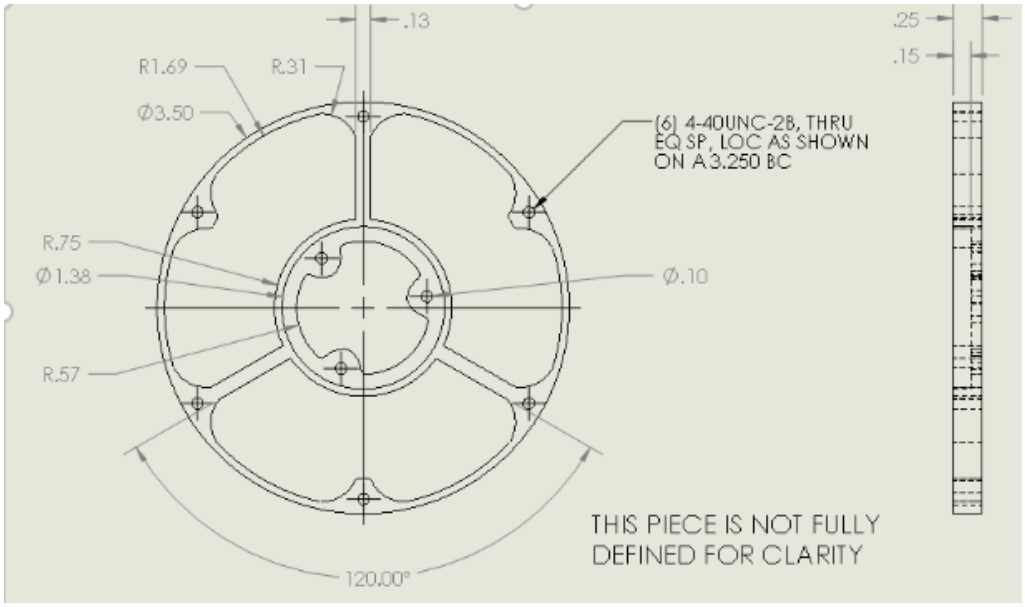

Figure 14: The SolidWorks design schematic for the new substrate holder, intended to replicate the exact size parameters of the original.

To verify that the new holder design would produce high enough temperatures and not compromise a consistent surface temperature, ANSYS thermal simulations were used. A baseline model was drawn in SolidWorks which includes the two quartz lamps, the original holder, and a wafer, all with idealized geometries (Figure 15). The steady-state thermal simulation was used to simulate internal heat generation of the lamps along with radiative heat transfer between all

surfaces, no conduction was used. The result of the baseline simulation roughly agreed with our experimental results, showing a maximum wafer temperature of 225 ˚C for a 500 ˚C setpoint.

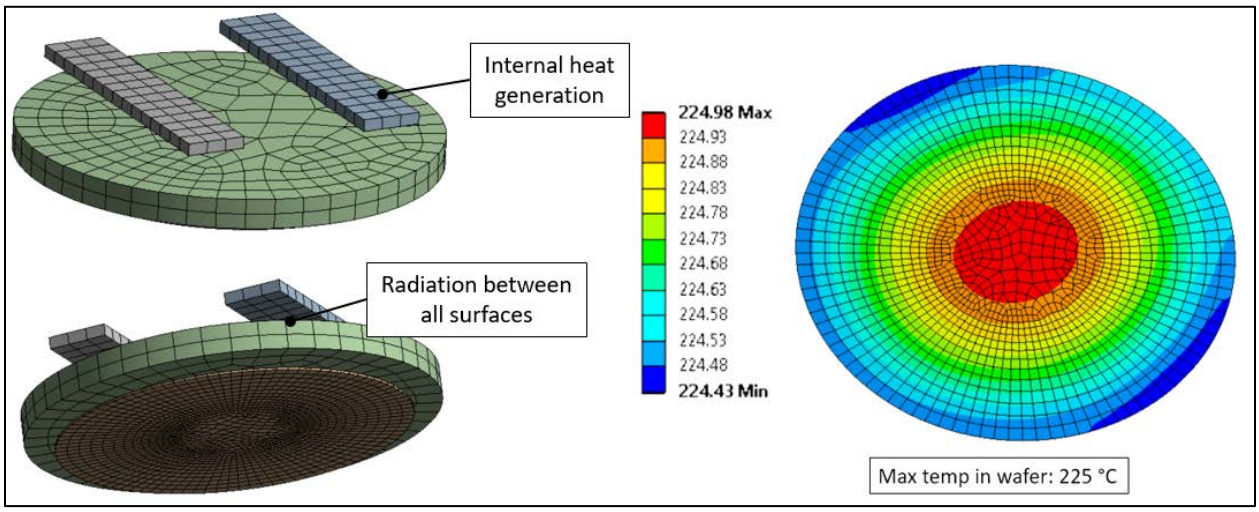

Figure 15: (Left) The SolidWorks original holder design transferred to ANSYS. The design includes an approximation of the quartz heat lamps geometry, the holder, and a silicon wafer. (Right) ANSYS thermal simulation results for the Si wafer, with the lamps at 500 ˚C. The maximum temperature reached was 225 ˚C, with the temperature value being very consistent across the wafer's surface.

The holder design seen in Figure 13 (b) was then implemented into the ANSYS thermal simulation under the same conditions as the original holder. Figure 16 (Right) shows the results of the simulation when the lamps were at 500 ˚C. The resulting maximum temperature was 282 ˚C. Although not ideal, the increase was significant enough to warrant further testing. One important consideration from the new holder's results was the increase in variation of temperature across the sample. Hot spots should be avoided because non-uniform stress is not described well by the Stoney equation and the MOSS does not have the ability to interpret it. The simulation, however,

is static and the actual sample holder will be rotating. Therefore, the SolidWorks model of the three-spoke holder design was commissioned to be 3D printed in Inconel 625.

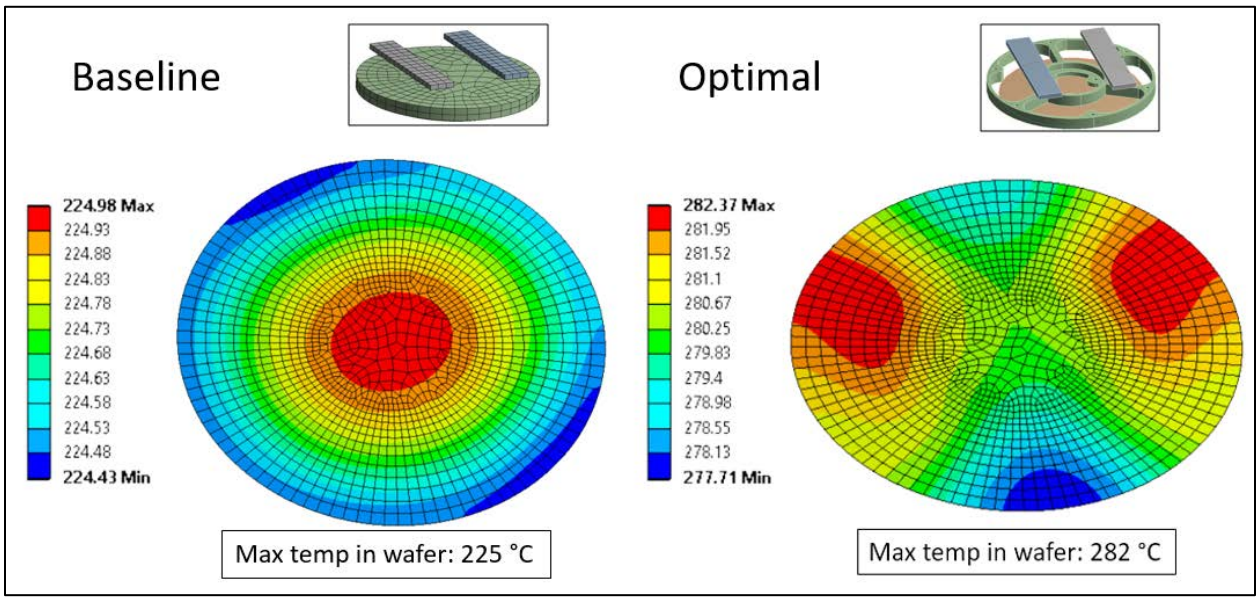

Figure 16: ANSYS thermal simulation results for the Si wafer using the original substrate holder (Left) and a new substrate holder (Right) with the lamps at 500 ˚C. The maximum temperature reached was 225 ˚C for the old holder and 282 ˚C for the new holder.

2.5 THERMAL CALIBRATION – THREE-SPOKE SUBSTRATE HOLDER

The new three-spoke substrate holder was placed with a wafer and attached thermocouple into the sputter system's main chamber. The objective of this experiment was to calibrate the actual substrate temperature to the heat controller reading based on the built-in thermocouple. The thermocouple was attached with ceramic adhesive to the center of the sample and connected to a

thermocouple feedthrough. The sample temperatures were recorded with a thermal datalogger. During the heating process, the sample was manually rotated ~270° back and forth as to not tangle the thermocouple or generate hotspots. Once again, the overall goal was to achieve sample temperatures greater than 300 °C, putting it in range for a Ta phase transformation.

A modification made to the previous calibration was using the ramp mode as opposed to setpoint mode. The ramp mode allows the user to set a ramp rate. Our goal was to see what ramp rates generated the highest temperatures or if it did not matter. A range of ramp rates were tested between 3 and 50 °C/min. An example of this experiment is shown in Figure 17 for the 25 °C/min ramp rate. The temperature of the sample and ramp rate are displayed versus time. After an initial spike and fluctuation in temperature, the sample temperature begins increasing linearly around ~160 °C. Having a linear relationship between temperature and time would make data analysis easier.

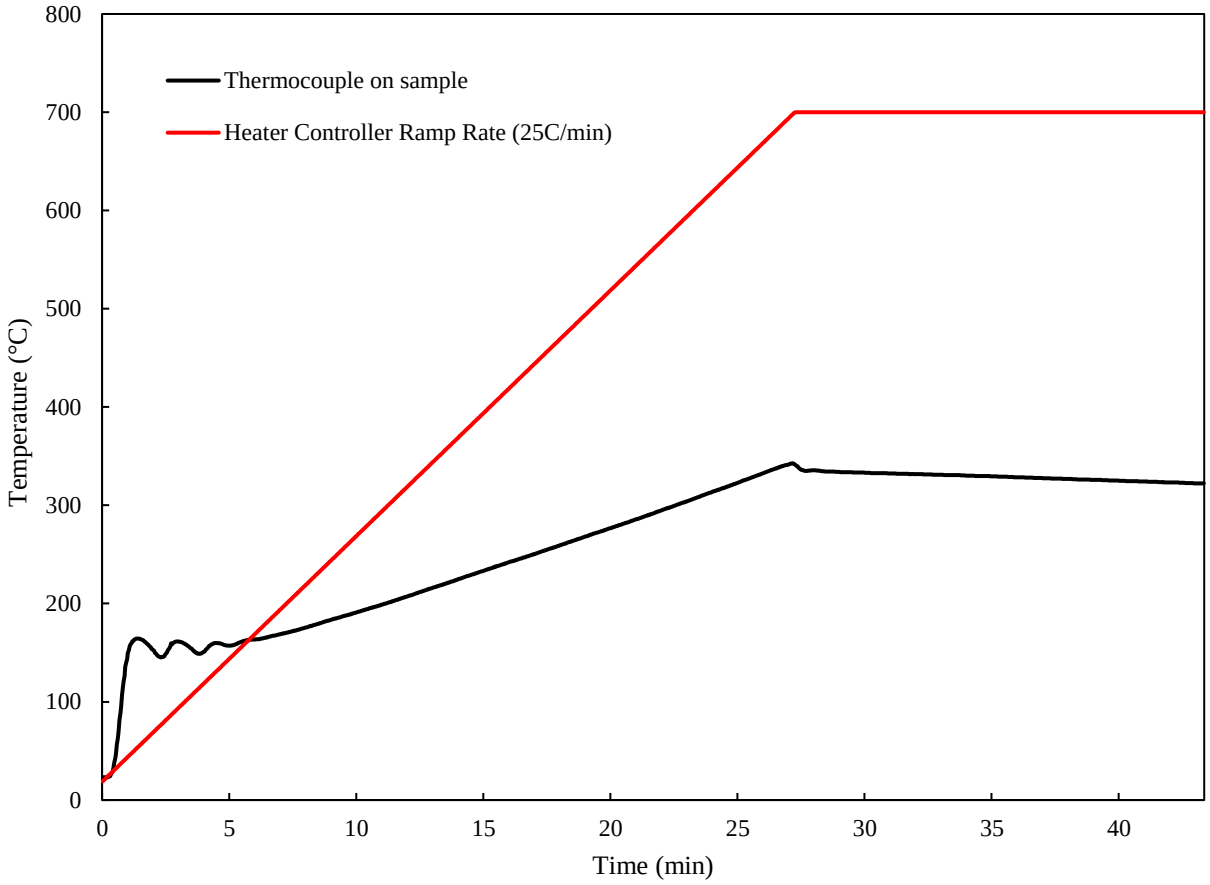

Figure 17: The temperature as measured by a thermocouple placed on the sample versus time. The ramp rate of the temperature for the sample is compared to that of the built-in thermocouple.

Each of the ramp rate test runs were plotted as sample temperature versus built-in thermocouple temperature as seen in Figure 18. All ramp rates eventually produce a linear regime for the sample temperature. The lower ramp rates have lower maximum temperatures and stabilize at lower temperatures. While the higher ramp rates are vice versa. The 25 ˚C/min ramp rate was chosen because it produced a high maximum temperature while stabilizing at a marginally higher temperature than the lower ramp rates. During the annealing steps in the experiment, the

temperature recorded will be from the built-in thermocouple. This result provides a linear relationship between the measured value and the actual sample temperature.

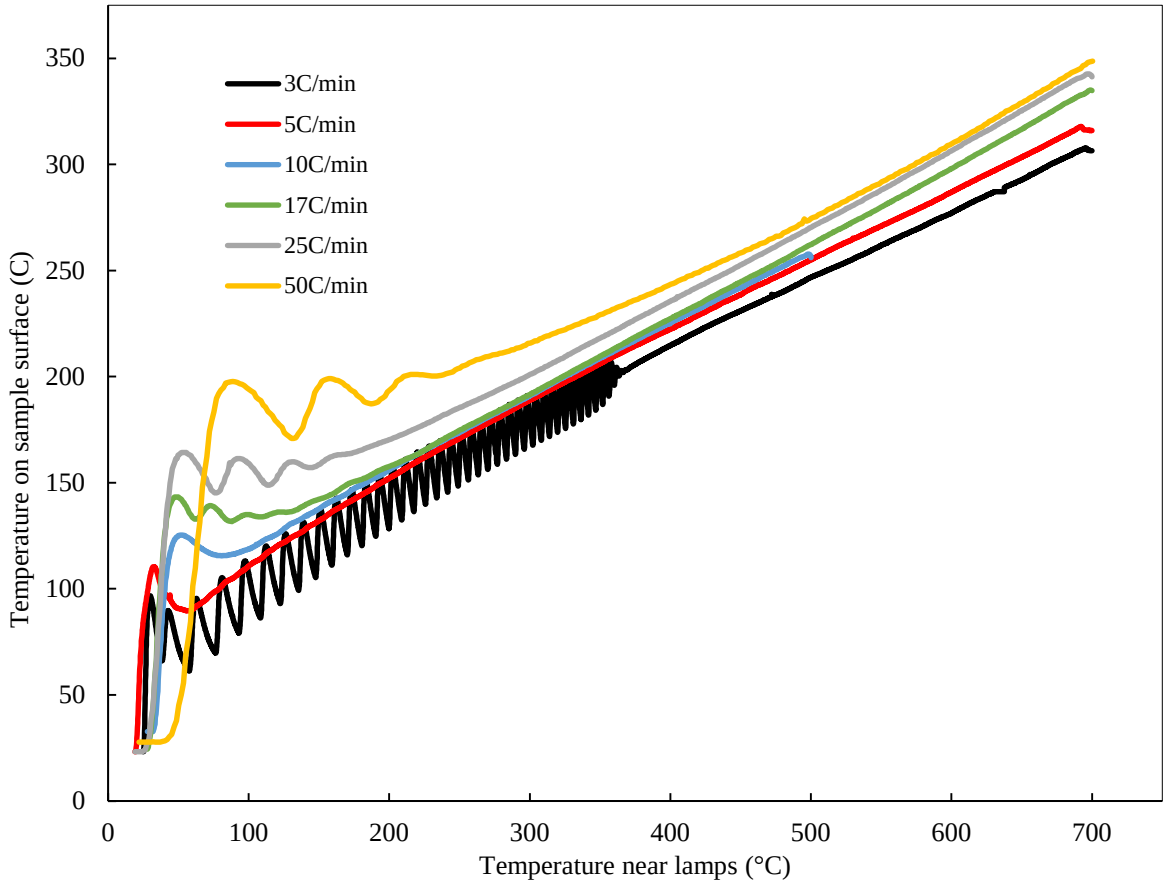

Figure 18: A comparison of a range of ramp rates for the heat controller. The temperature measured at the sample surface versus the temperature near the quartz lamps.

2.6 SPUTTER DEPOSITION AND HEAT TREATMENT

Tantalum thin films were deposited in a UHV DC magnetron sputter system. Samples were sputtered on (001) Si wafer with a 3" diameter and a 381 μm thickness. The samples were removed from the manufacturers packaging and immediately placed in the sample holder and into the load lock. Other than spray cleaning the wafer with N_2, no prior cleaning steps were taken. The samples were moved into the main deposition via the load lock arm. This was all performed at approximately the systems base pressure, $1x10^{-8}$ Torr. Within the main chamber are the sputter targets, heating lamps, and stress measurement tool. Once the substrate holder was attached to the rotation column, it was raised to the default deposition position. When ready to begin the deposition process, the substrate was rotated at ~10 rpm.

Plasma cleaning of the substrate was performed first. Plasma cleaning has been shown to remove organic contaminants from surfaces by sputtering the surface. The sputter species, Argon, is ionized in the plasma and electrically directed at the substrate. For the sputter cleaning process, a separate RF source of opposite bias was used. The ionized Ar atoms physically bombard the substrates surfaces removing contaminants. The downside to sputter cleaning can be implantation of the Ar atoms, substrate damage creating defects, and overall surface roughening. To avoid such negatives, the sputter power was set to 25 W and only run for 90 sec. The substrate rotating at ~10 rpm is an effort to avoid the plasma favoring a particular area of the substrate and causing additional damage.

Following plasma cleaning, the kSA MOSS software was initialized to begin taking stress measurements. For more details regarding this procedure see section 2.7 on the MOSS. During the time the MOSS gathers a flat reference and begins collecting data, the target was pre-sputtered.

Pre-sputtering a target is done to remove surface impurities and defects before exposing the sample. Sputtering impurities will result in impurities in the film while sputtering a target with crystalline defects can result in non-uniform deposits. For the pre-sputtering process, the main chamber pressure was brought to 8 mTorr. The DC magnetron power supply was then tuned to 35 W. Turning on the power struck a plasma and the shutter was kept closed for 5 minutes. At the end of the 5 min, pre-sputtering was transferred directly into the deposition procedure.

The purpose of this study was to investigate the dependence of α-Ta formation on thermal related processes like annealing and high-temperature depositions, so all other preparation and deposition parameters were kept constant throughout. After pre-sputtering, the DC power supply was increased to 200 W. The shutter to the Ta target was open and a timer for 17 min and 27 sec was started. These parameters were decided based on a previously determined sputter rate of 1.93 Å/sec and the desired thickness of 200 nm [49]. When the deposition was completed, the shutter was closed, power set to 0 W, and the Ar gas flow turned off. For heated depositions, the sample was heated to ~350 $^{\circ}$C during the plasma cleaning step. The annealing process began 15 min after deposition by turning on the heat controller. For details regarding each samples, heat treatment see Table 1.

Table 1: The samples used in our sputter deposition experiments and their respective heat treatments.

Sample Name	Heat Treatment
MC002-04	As-deposited (none)
MC002-05	Post-deposition annealing: 20→350 °C at 25 °C/min
MC002-06	Post-deposition annealing: 20→350 °C at 25 °C/min
MC002-07	Post-deposition annealing: 20→350 °C at 25 °C/min
MC002-08	Heated deposition: 350 °C during and held for 15 min following deposition
MC002-09	Heated deposition: 350 °C during and held for 15 min following deposition
MC002-10	Post-deposition annealing: 20→350→20 °C at 25 °C/min

2.7 MULTI-BEAM OPTICAL STRESS SENSOR

The primary use of the MOSS is seen in characterizing thin film stress during deposition and annealing. Two components of the kSA MOSS are shown in Figure 19 (a) and (b). The MOSS is located underneath the main chamber, where a glass panel allows optical access to the reflective surface of the sample. Connected to the rotation column on top of the main chamber is a trigger laser for the MOSS. Each rotation triggers the laser, which tells the kSA software to record a data point. The operating principle behind the MOSS follows directly from the discussion in section 1.3.3 on the Stoney equation.

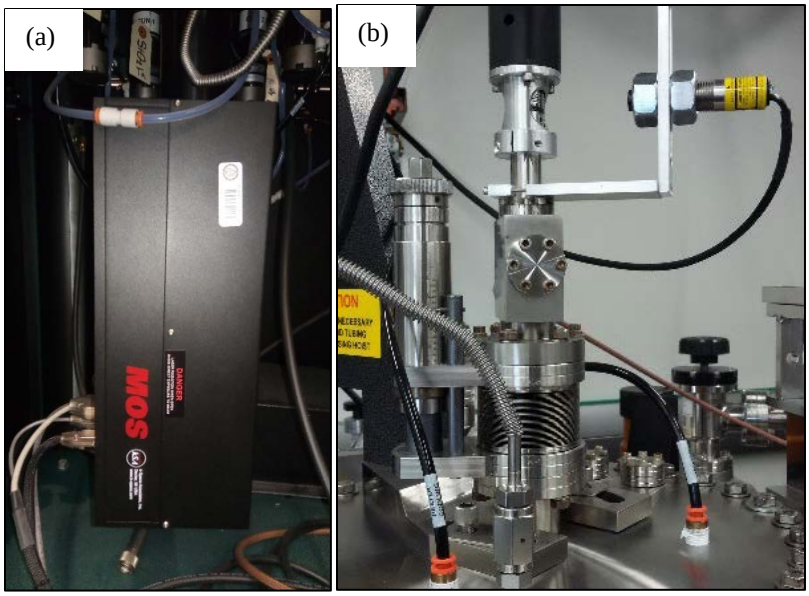

Figure 19: (a) The kSA MOSS attached to the bottom of the UHV sputter systems main chamber. (b) The trigger laser for the MOSS, facing the rotation column of the sputter system.

The first scenario in which MOSS was used was to measure the stress evolution of a thin film during deposition. Sample preparation followed standard thin film deposition procedures. Important details to note are that the substrate is not constrained in the direction normal to the MOSS and the face of the sample is reflective. Also, the substrate was rotated throughout deposition and heating processes.

In situ or relative stress measurements were used to monitor the sample continuously in real-time. Prior to the deposition beginning, a flat reference was taken. This acquires an initial beam-spacing that proceeding measurements can be compared to. For this method, the absolute change stress is not necessary. Each relative change in beam-spacing provides enough information to calculate the complete stress evolution during the process. The target cleaning step provided a

good opportunity to start the stress measurement collection. Once the sputter power was increased and the shutter was opened, the kSA software had already recorded several data points.

For some select samples, 15 minutes following the conclusion of the deposition, they were annealed. After the previous data was saved, a new data collection run was started, keeping the same flat reference. Once the kSA software began recording, the heat controller was initialized. As the sample was heated from room temperature to 350˚C, a stress evolution was recorded.

Following the deposition or anneal, the data collection can be stopped. What was saved was a series of substrate curvature measurements versus time. Using the Stoney equation, the raw data was converted to film stress, if the substrate thickness and deposition rate or film thickness were known.

2.8 FOUR-POINT PROBE

Tantalum thin films were electrically analyzed by a Jandel four-point microposition probe.

The four-point probe is an electrical characterization tool that measures the resistivity of semiconductor materials. Traditional multimeters utilize a 2-point probe method which is less accurate due to the lead and contact resistances contributing to the measurement. Four-point probes are used for greater accuracy as they can isolate the samples resistivity. The four-point probe utilizes four tungsten tips in a line that come into contact with the sample. The outer probes supply current, while the inner probes measure the voltage between contact points. Using this voltage and the set current the sheet resistivity can be calculated. There are two cases to consider when

calculating sheet resistivity, the film thickness is greater than the probe spacing, t>>s, and the film thickness is less than the probe spacing, t<<s. These ratios dictate the correction factor k.

$$\rho = k \times \frac{V}{I} \times t$$

Where ρ is the volume resistivity (Ω-cm), V is the measured voltage (V), and I is the supplied current (I), t is the thin film thickness (cm), and k is the correction factor [50].

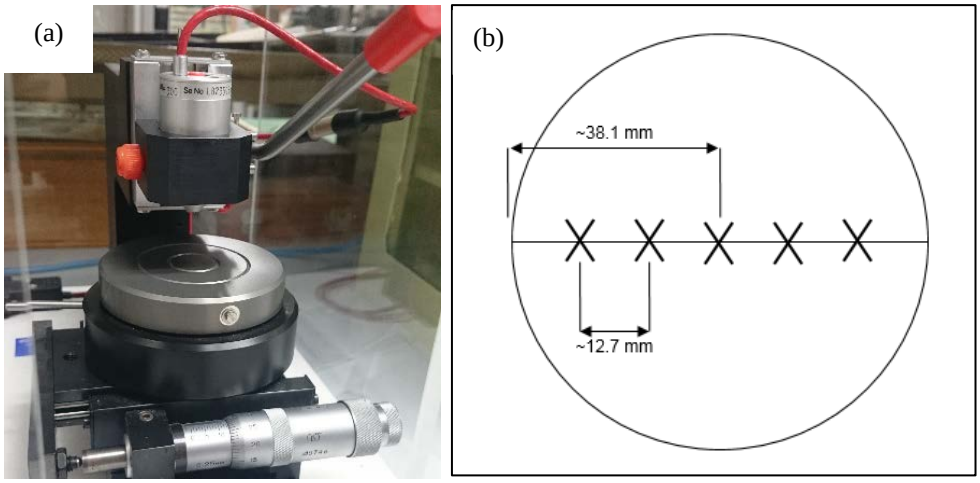

Figure 20: (a) The Jandel four-point probe. (b) The five positions where resistivity measurements were taken then averaged. [49]

To take a series of resistivity measurements, each sample was placed on the Jandel four-point probe stage and brought into contact with the probes. The current was set to 100 μA and the voltage was measured at five different positions across the sample, as seen in Figure 20 (b). These five measurements were averaged for an average voltage value for each sample. Resistivity was then calculated using the previously referenced equation.

2.9 X-RAY DIFFRACTION

2.9.1 Grazing Incidence X-Ray Diffraction

Grazing incidence x-ray diffraction (GIXRD) was used for phase identification of Ta thin films. GIXRD is the favored XRD technique for phase identification in thin film applications. The small incident angle of the x-rays avoids high-intensity substrate diffraction patterns. A PANalytical Empyrean x-ray diffractometer with a Co K_α source set to 40 kV and 40 mA was used, following grazing incidence diffraction procedures. The build for the GIXRD setup began with the Co K_α source and PreFIX module optics. In the incident beam path, there was the parallel beam x-ray mirror for Co radiation, along with the Soller slit (0.04 rad) and divergence slit (1/32”). Additionally, a beam attenuator was used during calibration. The wafer was centered on the χ-φ-z stage with a 6” circular mount. The PreFIX module of the diffracted beam path held a parallel plate collimator and Soller slit (0.04 rad). Lastly, a PIXcel^{3D} solid-state pixel detector was used.

Several calibration steps are required before GIXRD measurements can be performed on the sample. First, the direct beam intensity was established without the sample. Then, with a mounted sample, the stage was moved in the z-direction until the measured intensity is 20-50% of the direct beam. This placed the sample in the beamline. Next, the grazing angle, omega, was optimized. This was done using the most intense diffraction peak of a 2θ scan and scanning omega. The highest intensity omega value was identified and then used for the final 2θ scan. The grazing incidence angles all fell within a range of 0.7-1°. The full scans were run in continuous line mode

with a receiving slit active length of 14.025 mm. The scan settings were a range of 2θ values from 20-80° with a step size of 0.07° and 3.52 sec per step. Three samples were tested with GIXRD, the as-deposited, the post-deposition annealed, and the high-temperature deposition.

2.9.2 Asymmetric Powder X-Ray Diffraction

Asymmetric powder x-ray diffraction (PXRD) was used for phase identification and analysis of Ta thin films. The (100) Si substrates have a strong (400) diffraction peak at 2θ = 82.4° that can overlap with the (112) α-Ta and (400) β-Ta peaks. To avoid the Si signal, a +1.5° ω offset was applied to the film normal. A PANalytical Empyrean x-ray diffractometer with a Co K_α source set to 40 kV and 40 mA was used for asymmetric ω-2θ scans. The PXRD setup began with the Co K_α source and PreFIX module optics. In the incident beam path, there was the fixed divergence slit module, the fixed divergence slit (1/4°), the anti-scatter slit (1/8°), a 10 mm mask, and Söller slits. Additionally, a beam attenuator was used during sample height calibration. The wafer was centered on the χ-φ-z stage with a 6" circular mount. The PreFIX module of the diffracted beam path held an anti-scatter slit, Söller slits, and a Fe K_β filter. Lastly, a PIXcel solid-state pixel detector was used in scanning line mode.

Several calibration steps are required before PXRD measurements can be performed on the sample. With a mounted sample, the stage was moved in the z-direction until the measured intensity is 50% of the direct beam. An ω offset of +1.5° from the film normal was used for the ω-2θ scans. The final scans were run in continuous line mode. The scan settings were a 2θ range of 20-120° with a step size of 0.026° and 0.75 sec per step. With the instrument in the PXRD

configuration, three samples were tested, the as-deposited, the post-deposition annealed, and the high-temperature deposition.

2.10 X-RAY PHOTOELECTRON SPECTROSCOPY

X-ray photoelectron spectroscopy (XPS) was performed on Ta thin films for elemental composition analysis with the goal of determining film thickness. Combined with ion milling, the thickness and evolving composition of the films could be better understood. Three types of Ta thin film samples were used in these experiments. All samples were deposited via UHV magnetron sputtering on Si substrates. The first was β-Ta with as-deposited conditions. The other two samples were α-Ta which were processed at high temperatures.

The XPS instrument used in these experiments utilizes an Al K_α source with an x-ray energy of 2000 eV combined with an integrated ion milling system. The experiments began with a survey that scans for all elements as an overview. Then, elements of interest were scanned for by the software identifying specific electron orbitals. The elements of interest were Ar, O, Si, and Ta. First, the survey and elemental scans were performed and then ion milling would remove a ~7.2 nm layer of film. A spot size of 500 μm was used as 40 scans were performed on each sample. The analyzer was set to constant analyzer energy (CAE) mode with an electron pass energy of 50 eV. Approximately ~300 nm of the samples were milled, removing the film and entering the substrate.

3.0 RESULTS

In this section, the results from multiple tantalum thin film studies will be presented. The MOSS stress evolution of during deposition and annealing, XRD phase analysis including glancing angle and asymmetric of each type of sample, and XPS depth profiles.

3.1 STRESS

Figure 21 shows the biaxial in-plane stress of a Ta thin film during deposition as a function of time. The stress was calculated using the Stoney equation and the raw substrate curvature data recorded by the MOSS. This sample represents a batch of Ta thin films that were all deposited under the same conditions as described in section 2.6. In particular, the depositions were not externally heated. The initial variation in stress was due to very small film thickness and sample curvature values. Specifically, the curvature values before deposition can be small negative or positive values when compared to the flat reference. This leads to a large variance in values when calculating stress with the Stoney equation. Before deposition began, there was a 5 min pre-sputter process. Therefore, the stress values before the 5 min mark can be disregarded. Once deposition began, the film thickness was approximated to increase linearly in accordance with a determined deposition rate. The measured substrate curvature increased linearly, corresponding to island nucleation and growth. Compressive stress increased until a steady-state value of ~2 GPa was reached, where both film thickness and curvature increase at the same rate.

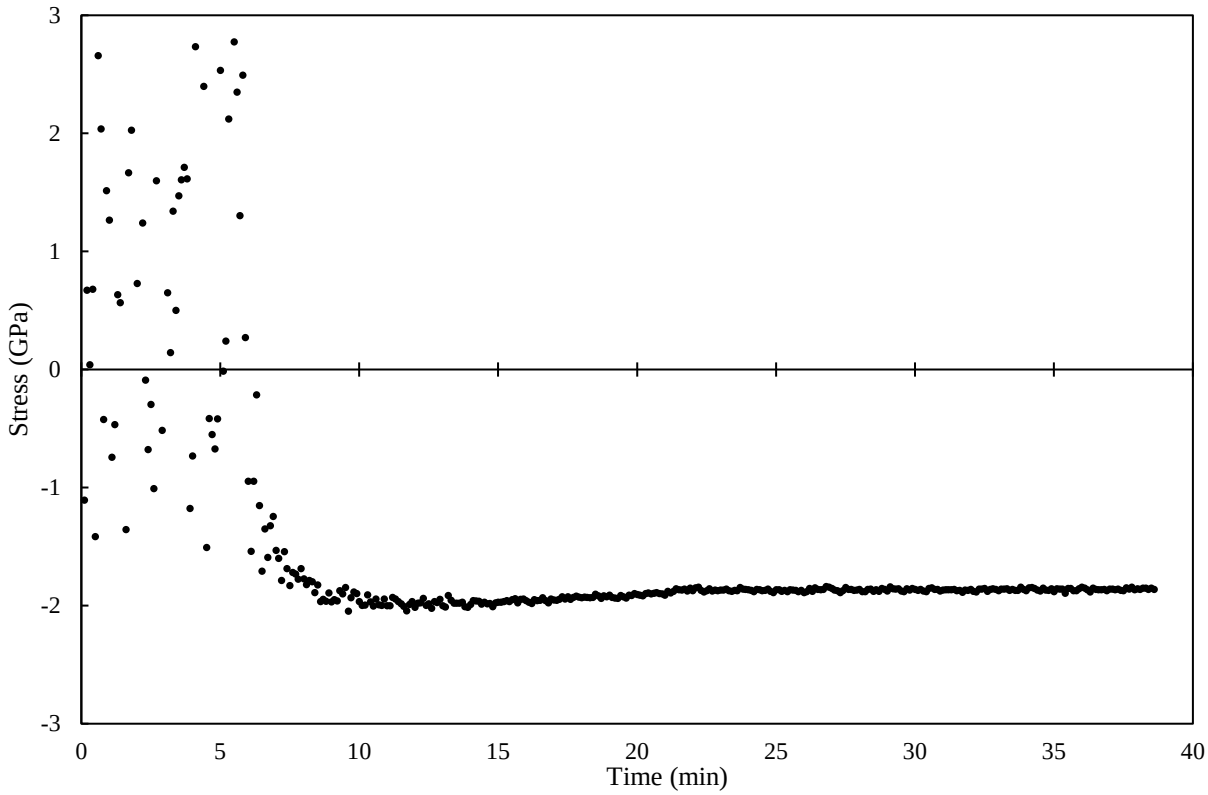

Figure 21: The biaxial in-plane stress versus time for an as-deposited Ta thin film deposited via sputtering.

Figure 22 shows the biaxial in-plane stress of a Ta thin film during heated deposition as a function of time. Again, the stress was calculated using the Stoney equation and the raw substrate curvature data recorded by the MOSS. This sample was deposited under heated conditions. This means prior to deposition; the substrate was heated to 350 ˚C and held there throughout. The initial variation in stress was due to very small film thicknesses and the fluctuations of the quartz heating lamp. This issue will be discussed in further detail with regards to the annealing process.

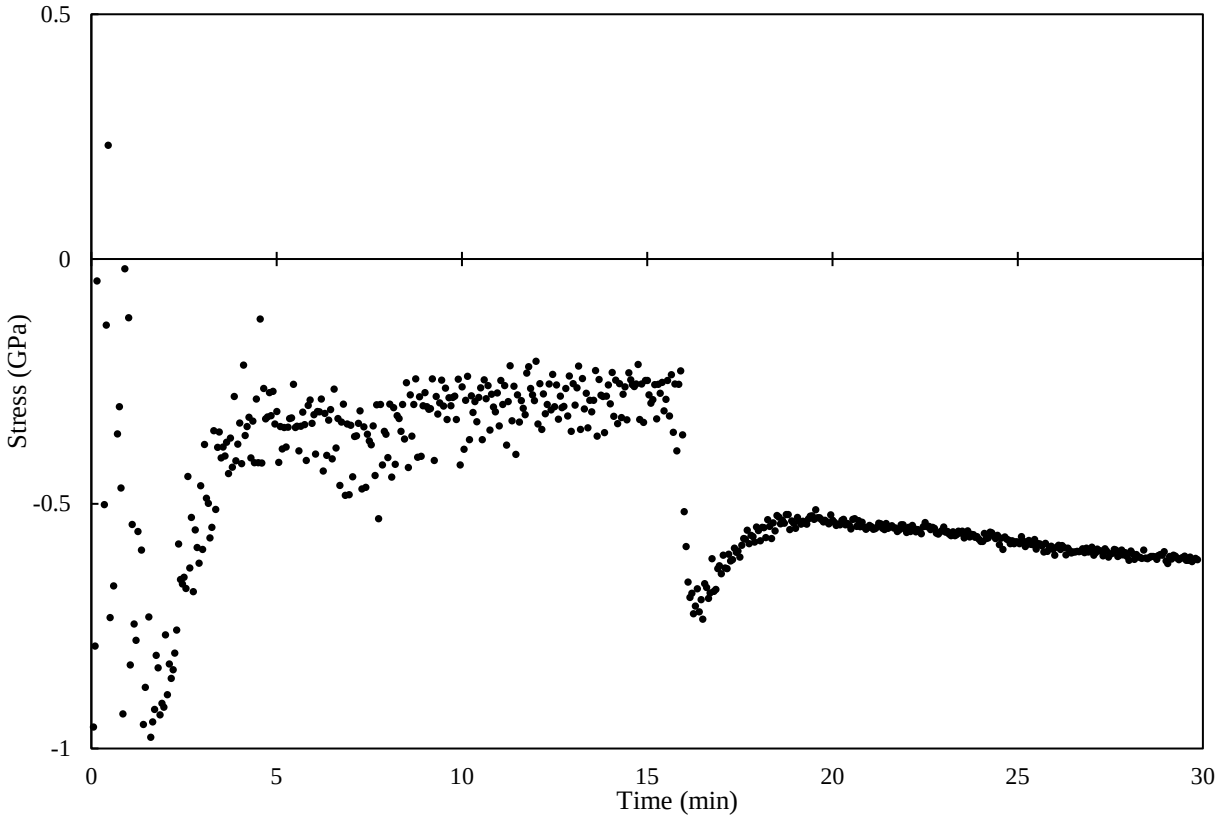

Figure 22: The biaxial in-plane stress versus time for heated deposition of a Ta thin film deposited via sputtering.

Figure 23 shows the biaxial in-plane stress of Ta thin films during annealing as a function of temperature. The films were annealed between room temperature and 350 ˚C, 15 minutes after the deposition process had ended. For annealing, the pressure in the main chamber was brought back down to the base pressure of $1x10^{-8}$ Torr. Around room temperature, the stress in the as-deposited films corresponds to the compressive stress of 2 GPa seen at the end of the deposition process. The large variation in stress values was due to the quartz heating lamp fluctuating on and off. This was primarily seen during the heating portion of the cycle due to the lamp overheating the sample then shutting off. A general trend during the early heating stage was the slight increase in compressive

stress. This can be attributed to thermal mismatch between the substrate and film. Between 225-250 °C, there was a significant change in the tensile stress direction of approximately 1.5 GPa. This corresponds with a phase transformation from tetragonal β-Ta to bcc α-Ta. Above 250 °C, the thermoelastic behavior continues with compressive stress increasing with temperature. At the maximum temperature, the cooling stage was handled in two different manners. First, uncontrolled cooling was performed. This means, at the maximum temperature, the quartz heat lamps were shut off permanently. Second, controlled cooling was performed. This is where the setpoint in the heat controller was set to ~20 °C. Regardless of the method, the samples experience a large change stress at the maximum temperature and end with the same stress at room temperature. The uncontrolled cooling sample experienced a more rapid cool down, but with less variation in stress. While, the controlled cooling sample experienced greater variation in stress, but with a slower cool down.

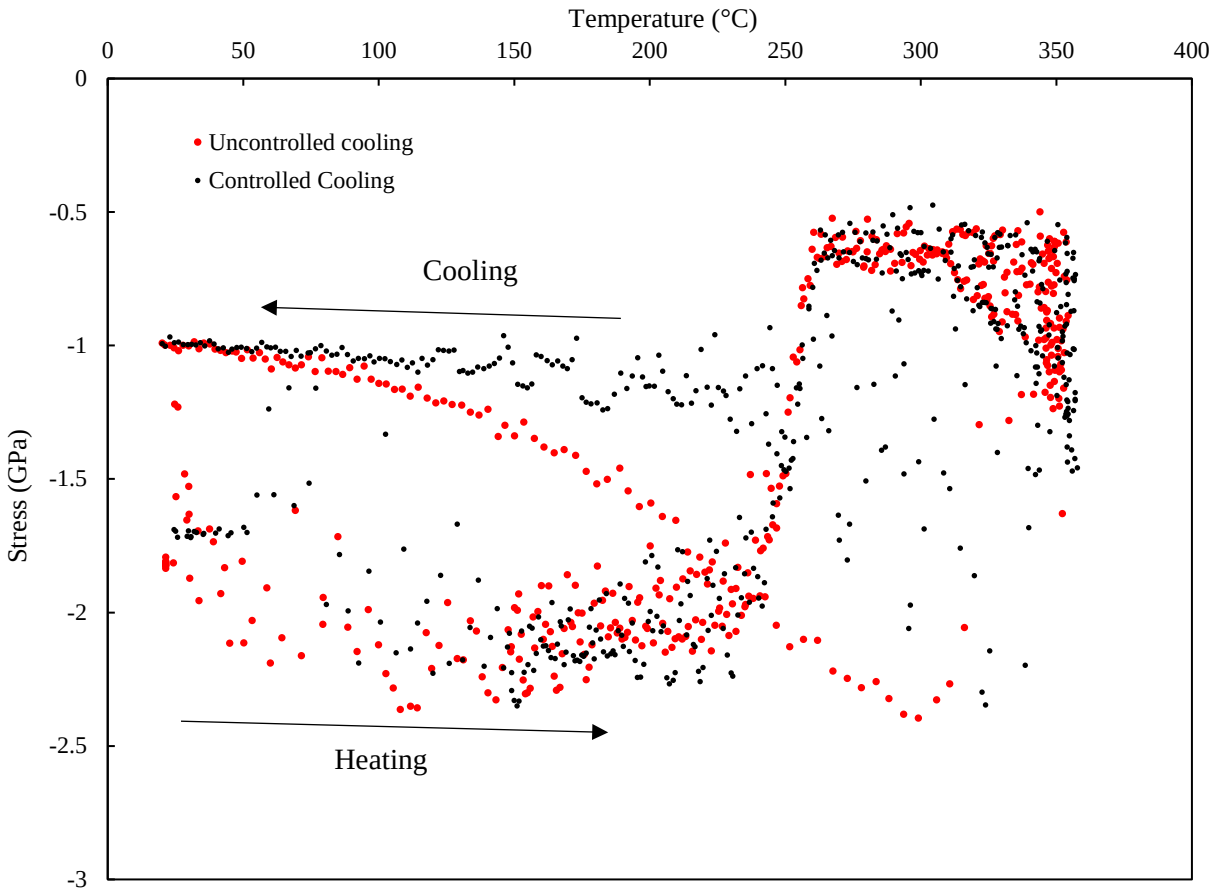

Figure 23: Biaxial in-plane stress versus temperature of the sample for Ta thin films deposited at room temperature via sputtering. Annealing occurred post-deposition, with samples either having controlled or uncontrolled cooling.

3.2 PHASE ANALYSIS

The heat treatments and resulting resistivity calculations of all Ta thin films are tabulated in Table 2: The samples used in our sputter deposition experiments and their respective heat treatments. A four-point probe was used to measure the resistivity of each sample. Four-point probe resistivity measurements were performed for each sample on five different areas of the samples and averaged.

The calculated resistivity changes drastically when a type of thermal process is performed on the Ta thin film. As-deposited Ta can be identified as β-Ta from its characteristically larger resistivity of 220 μΩ*cm. Both annealed and heated deposition Ta can be identified as α-Ta from the lower resistivity of approximately 20 μΩ*cm.

Table 2: The samples used in our sputter deposition experiments and their respective heat treatments. A four-point probe was used to measure the resistivity of each sample.

Sample Name	Heat Treatment	Resistivity (μΩ*cm)
MC002-04	As-deposited (none)	219.98
MC002-05	Post-deposition annealing	25.19
MC002-06	Post-deposition annealing	21.20
MC002-07	Post-deposition annealing	19.39
MC002-08	Heated deposition	18.12
MC002-09	Heated deposition	18.15
MC002-10	Post-deposition annealing	19.21

GIXRD measurements revealed that heat treated films show only α-Ta peaks and that as-deposited show β-Ta peaks. In Figure 24, both as-deposited and heat-treated Ta films diffraction intensities are displayed over a 20-80 ° 2θ range. The as-deposited film diffractions peaks suggest a (002) texture, but further confirmation with oPXRD is necessary.

Figure 25 shows the as-deposited diffraction peaks in more detail, identifying the various crystal orientations across the same 2θ scale. The heat-treated films show that high-temperature

processing will promote α-phase over the β-phase. From this 2θ range, the α-Ta texture is not well defined with both (110) and (200) orientations present [51] [52]. Also present in the heat treated XRD patterns are tantalum silicide ($TaSi_2$) diffraction peaks. The β-Ta pattern is represented in greater detail in Figure 25.

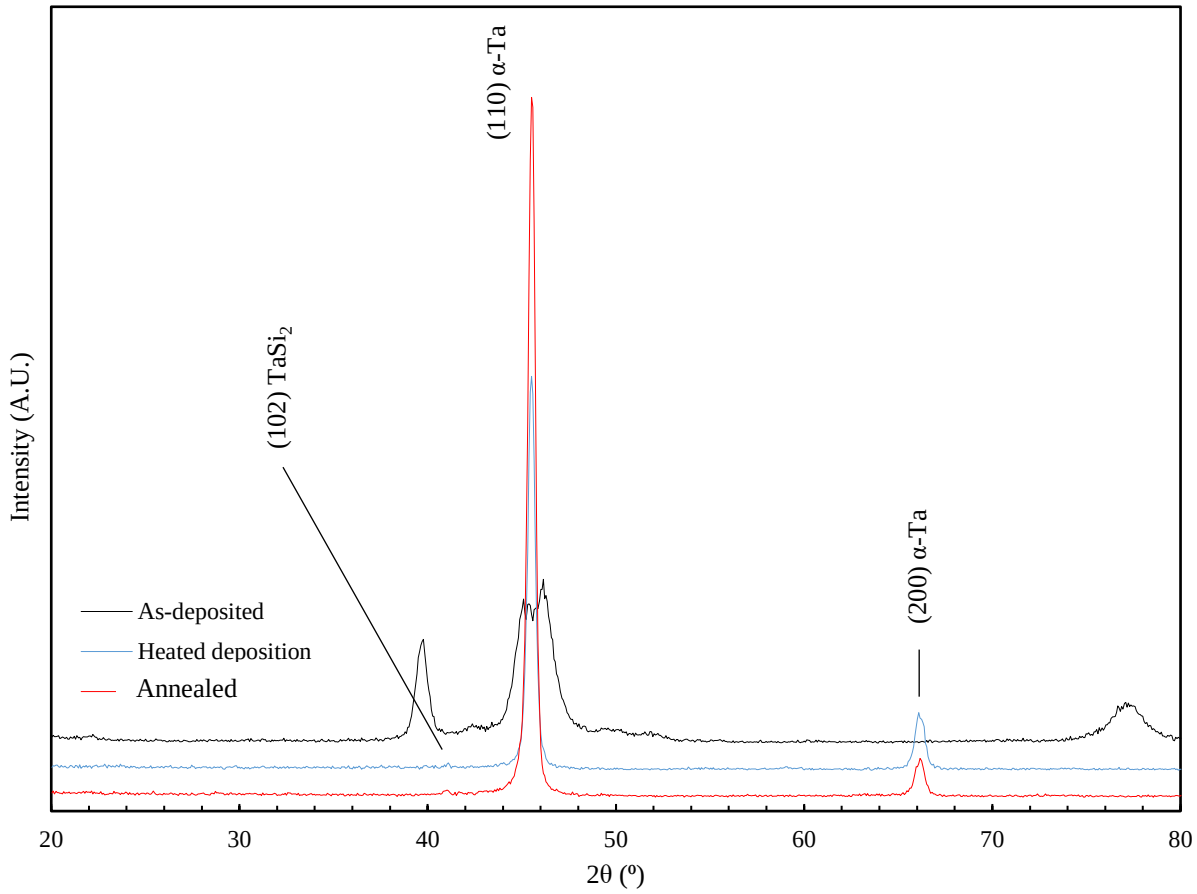

Figure 24: GIXRD Ω-2θ scans of as-deposited, annealed, and heated deposition Ta thin films. The (011) and (002) α-Ta peaks are visible. The β-Ta peaks are examined in more detail following.

The GIXRD measurements shown in Figure 25 are of as-deposited Ta thin film showing an array of textures. This pattern confirms the presence of β-Ta; however, GIXRD is not suitable

for identifying texture [23] [53]. The large area of irradiation and low penetration depth provided by the GIXRD setup avoids the substantial substrate peak but observes crystal planes non-parallel to the surface. The “evanescent” wave created by the critical incident angle moves parallel to the surface, while the detector is rotated. As a result, GIXRD was performed expressly to confirm the presence of α- or β-Ta.

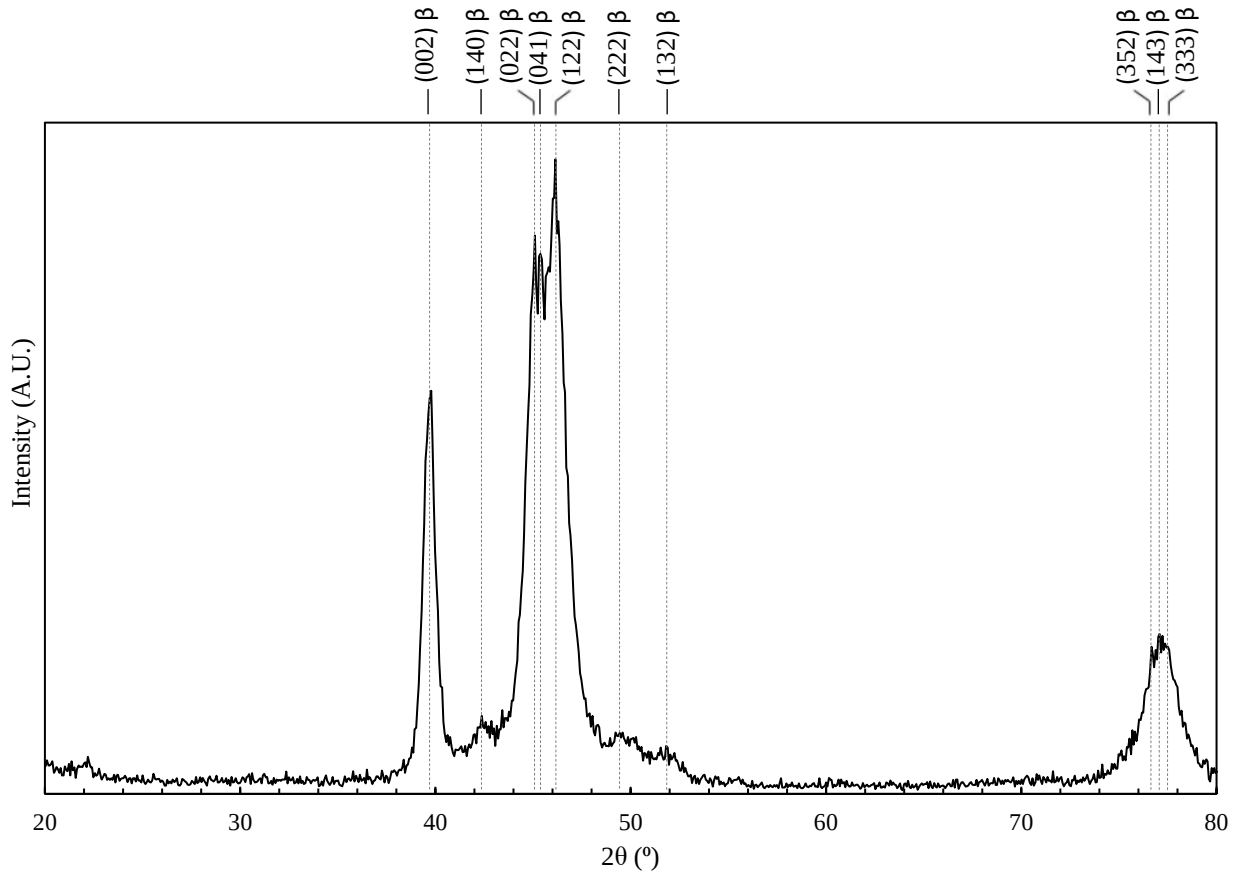

Figure 25: GIXRD Ω-2θ scans of the as-deposited Ta thin film.

The asymmetric PXRD measurements shown in Figure 26 display both as-deposited and heated deposition Ta thin films. Similar to the GIXRD results, the heat-treated sample is α-Ta with multiple crystal orientations present. Additionally, the $TaSi_2$ diffraction peaks are visible. Unlike

the GIXRD results, the as-deposited sample clearly shows β-Ta in the (002) orientation. This will be discussed in further detail in Section 4.2.

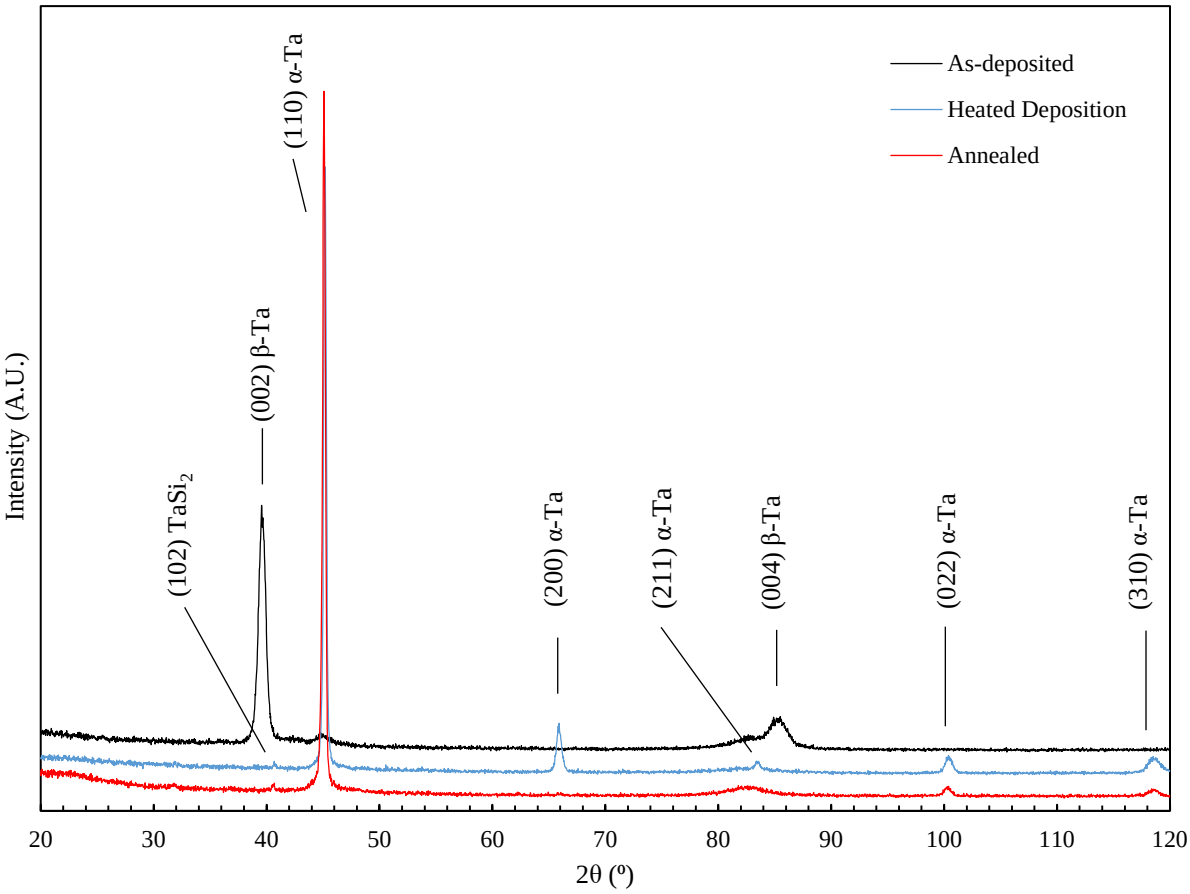

Figure 26: Asymmetric PXRD symmetric ω-2θ scans of as-deposited and heated deposition Ta thin films. Only (002) and (004) β-Ta peaks are visible for the as-deposited samples at this intensity scale. All α-Ta bcc reflections are visible.

3.3 X-RAY PHOTOELECTRON SPECTROSCOPY

An XPS survey of an as-deposited Ta thin film is shown in Figure 27. Similarly, Figure 28 and Figure 29 are XPS surveys, but of the annealed and heated deposition Ta thin films, respectively. A range of depths at which the XPS scanned was made possible by ion milling. This allows investigation of the elemental composition at varying depths throughout the film and substrate. The XPS survey displays the intensity of the analyzed photoelectron versus the binding energy of that electron. These peaks were identified by their characteristic binding energies as they correspond to specific electron configurations of certain elements and compounds. The detailed results regarding these figures are in Table 3.

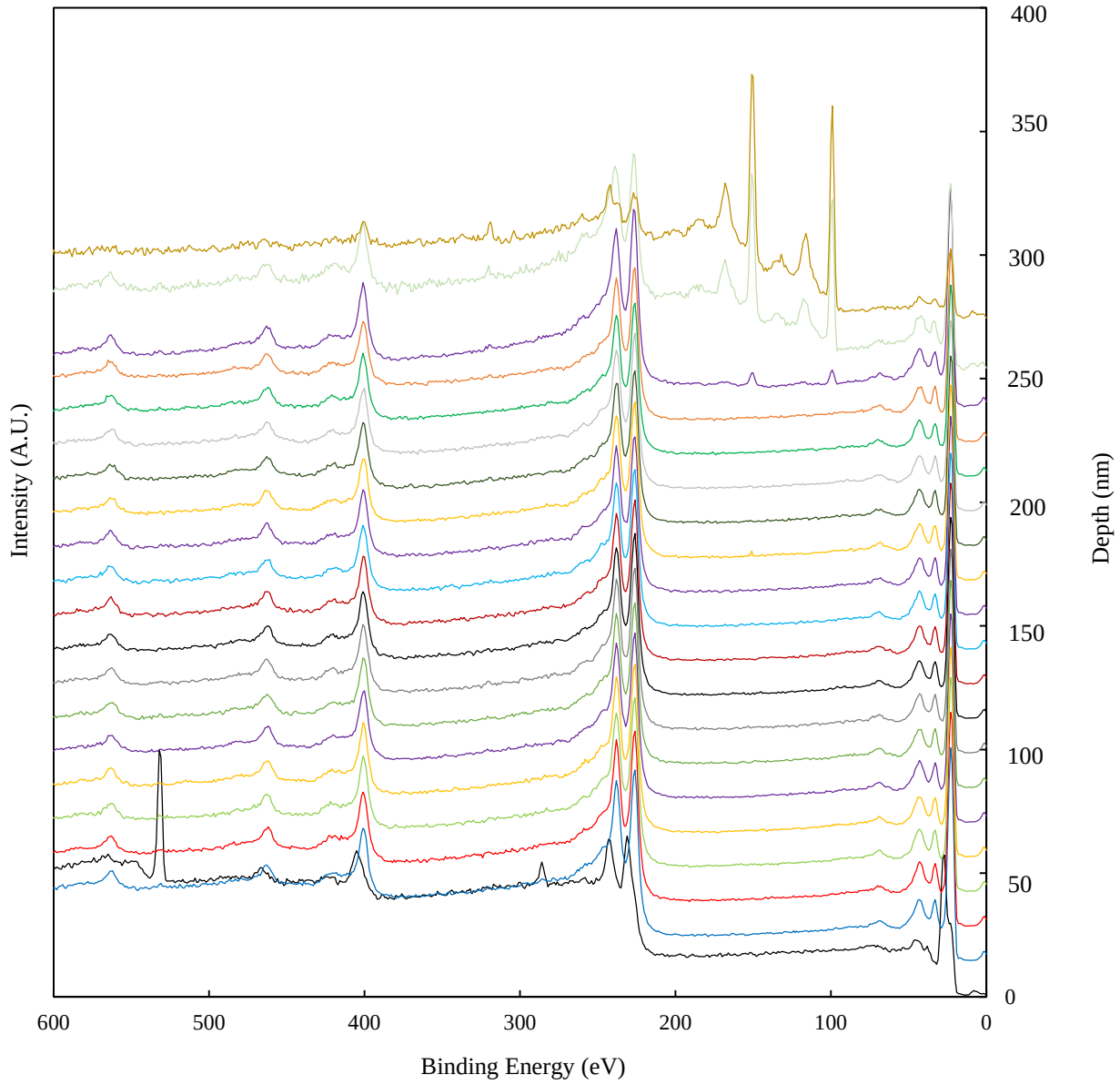

Figure 27: An XPS survey of an as-deposited Ta thin film displaying intensity versus binding energy. 20 scans were performed, where ion milling was used between scans to reach layers beneath the surface.

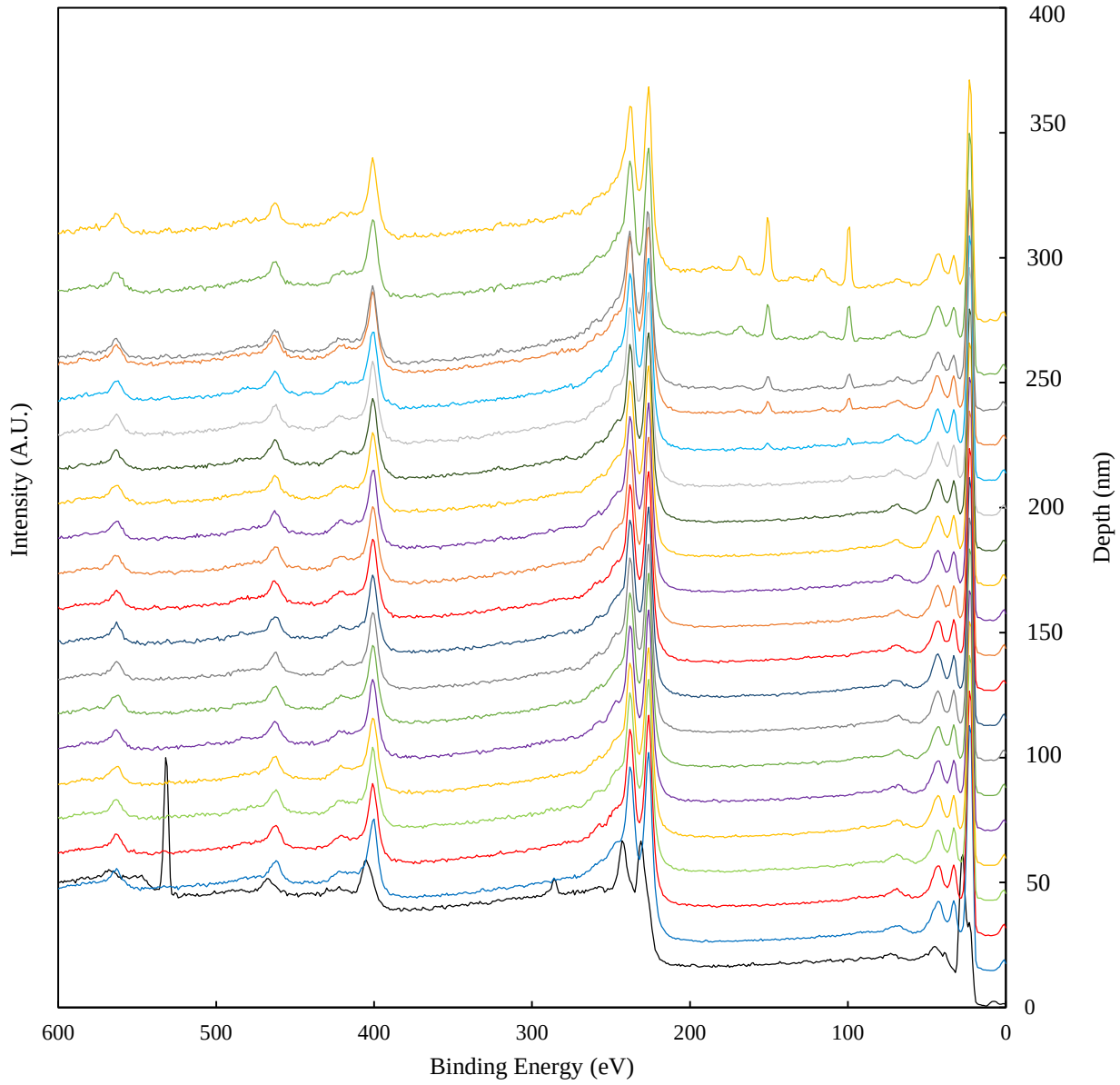

Figure 28: An XPS survey of an annealed Ta thin film displaying intensity versus binding energy. 20 scans were performed, where ion milling was used between scans to reach layers beneath the surface.

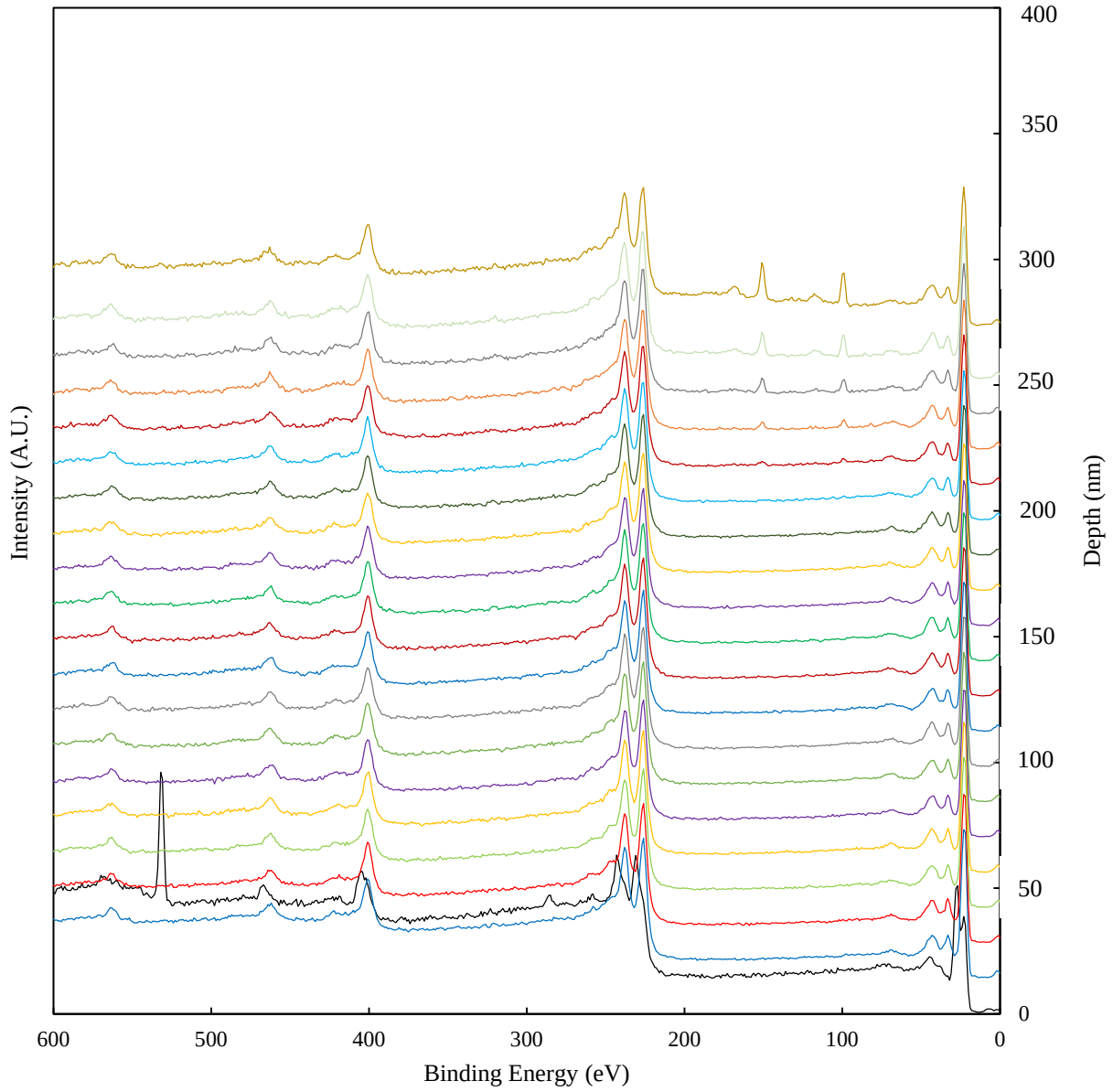

Figure 29: An XPS survey of a high-temperature deposition Ta thin film displaying intensity versus binding energy. 20 scans were performed, where ion milling was used between scans to reach layers beneath the surface.

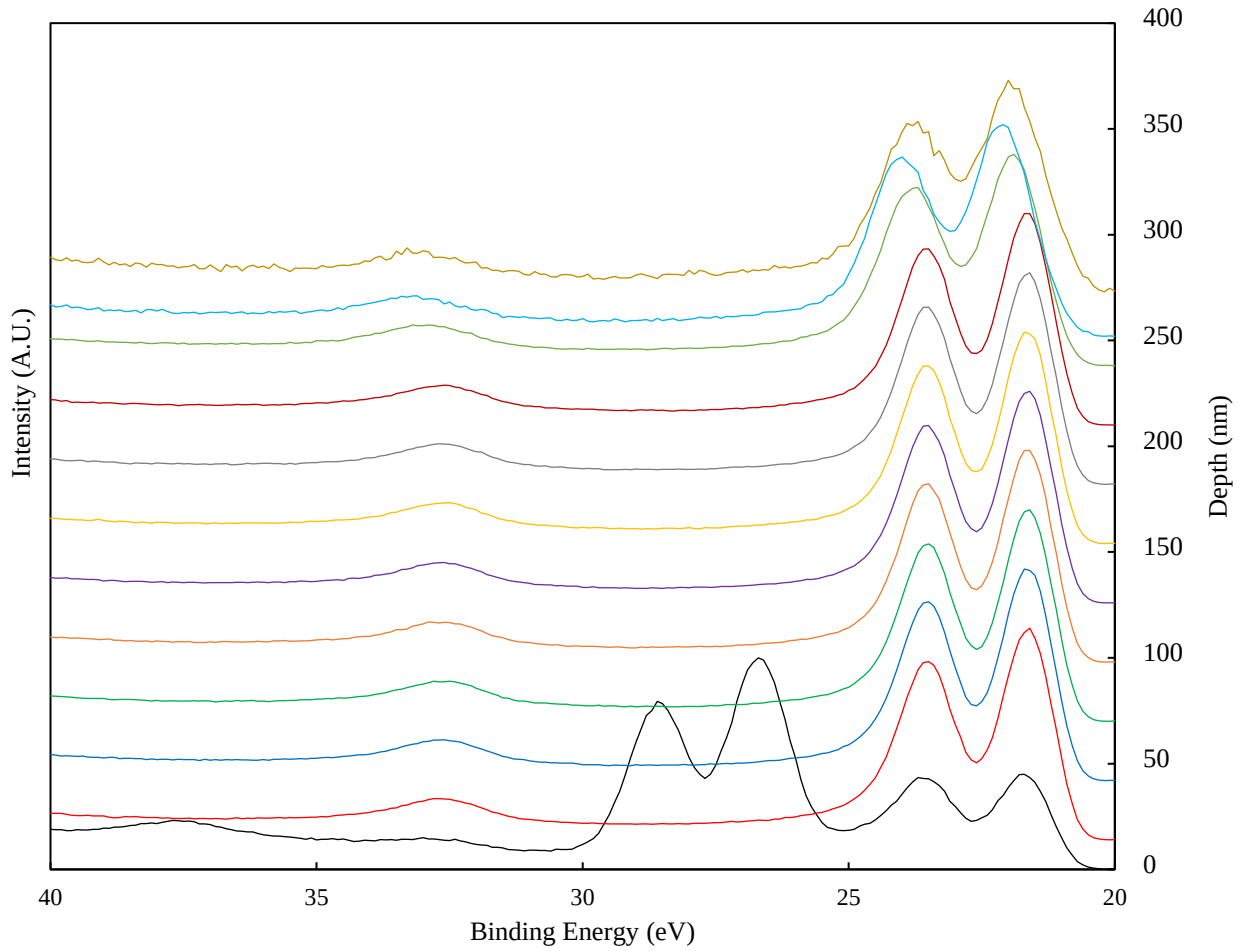

Figure 30: An XPS scan of the Ta 4f electron configuration displaying intensity versus binding energy for an as-deposited Ta thin film sample. The depth of the XPS scan is also displayed.

Table 3 holds the binding energy peak data from Figures 27-30. An XPS spectra handbook was used to identify specific electron configuration of elements [54]. The peak positions in Figures 27-29 do not change position based on how the samples were processed; however, the depths at which the peaks appear do. Figure 30 is an XPS scan of the Ta 4f electron configuration. This scan is a more precise measurement when compared to the surveys, meant to confirm the presence of Ta. As a result, both the 4f7 and 4f5 Ta electron configurations are visible throughout the film and

substrate, with binding energies of 21.6 and 23.5 eV, respectively. At the surface, a native tantalum oxide, Ta_2O_5, exists with a binding energy of 26.8 eV.

Table 3 also includes depth data representing when the binding energy peak appears in the sample cross-section. This was done to verify the film thickness and identify differences between the processing methods. From the as-deposited scan in Figure 27, a Si peak is present on the 35^{th} scan meaning approximately 250 nm had been milled away. Both the annealed and heated deposition samples showed Si peaks sooner, after their 30^{th} scan, approximately after 200 nm had milled away. This suggests the presence of tantalum silicide which is confirmed by XRD.

Table 3: Binding energy peak details identified in Figure 27-30 and cross-referenced with the XPS spectra handbook [54]. The binding energy peaks corresponding electron configuration and depth at which they are seen in the samples are tabulated.

Element/Compound	Electron Configuration	Binding Energy (eV)	Depth (nm)
Ta	4f7	21.6	All
Ta	4f5	23.5	All
Ta_2O_5	-	26.8	Surface
Ta	5p3	32.6	All
Ta	5s	67.8	All
Si	2p	100.4	225-300
Si	Plasmon loss	116.2	225-300
Si	2s	152.9	225-300
Si	Plasmon loss	167.9	225-300
Ta	4d5	226.1	All
Ta	4d3	237.6	All
Ar	2p	242	225-300
Ar	2s	319.5	225-300
Ta	4p3	400.6	All
Ta	Plasmon loss	420.4	All
Ta	4p1	462.5	All
O	1s	530	Surface
Ta	4s	562.8	All

4.0 DISCUSSION

In this section, the stress evolution, phase analysis, and XPS results of each sample type are discussed. When applicable, our results are compared to literature with similar studies.

4.1 STRESS

Sputter deposition of Ta thin films at room temperature resulted in compressive stress as seen in Figure 21. The development of compressive or tensile stress has been related to sputter pressure and incident particle energy in past studies [7] [34] [35] [36] [43] [55] [56] [57]. The trend seen in these studies connects compressive stress to high incident particle energy and therefore low sputter pressure. High incident energy has been shown to create self-interstitial defects in the thin film [57]. Throughout our depositions, the sputter pressure remained constant at 8 mTorr. Previous studies agree with our results of compressive stress of ~2 GPa at this sputter pressure [7] [43].

High-temperature sputter deposition resulted in a smaller compressive stress when compared to the as-deposited samples, as seen in Figure 22. To our knowledge, the *in-situ* stress evolution of heated Ta thin film deposition has not been previously investigated. Preheating the substrate to promote α-Ta growth has been experimented with [28] [32] [58]. These sources cite the presence of oxygen or hydroxyl groups as nucleation sites for β-Ta. Heated depositions change the substrate temperature during growth, affecting how the vapor phase forms a film. To begin

forming a film, the vapor phase must supersaturate the surface. At high temperature, adatoms often exceed the energy of attachment, meaning they evaporate. The increase in evaporation of adatoms at high deposition temperatures results in a lower net deposition flux [12]. However, later XPS results will show, heated deposition and annealed samples have similar film thicknesses.

An issue with this experimental setup is the development of thermal gradients in the sample, due to the quartz heating lamps fluctuating in intensity. The variation in stress values throughout deposition can be attributed to the lamps attempting to maintain a constant temperature. After the depositions were completed, the heating lamps shutting off results in a more intense thermal gradient in the sample. This can be seen in the quick increase in compressive stress after the 15 min mark shown in Figure 22. This is where a distinction is necessary between substrate curvature due to thermal gradients or thin film growth.

Annealing of room temperature Ta thin film deposition resulted in stress evolution that resembles other cases in literature. Shown in Figure 31 is a comparison between our Ta film and Clevenger *et al*. Ta film both annealed. This comparison highlights the limitations of our experimental setup. The variation in stress values due to the heating method limit our ability to identify regions of elastic and plastic deformation accurately. This includes the turn-around at the maximum temperature which has even larger variations. However, general trends can still be analyzed to find similarities.

After sputter deposition, the intrinsic stress of the Ta thin film is -2 GPa (compressive). In Figure 31 (a) between 0-150 °C, there is an increase in compressive stress which can be attributed to thermoelastic behavior. In Figure 31 (b), Clevenger *et al*. were able to calculate the Young's Modulus of the Ta film due to the linearity of this region of elastic deformation [7]. The variation in stress values prevents us from gathering similar mechanical parameters from β-Ta.

In Figure 31 (a) between 150-250 °C, there is stress relaxation which can be attributed to plastic deformation. Over this range, stress values change from -2.25 to -1.80 GPa. Here, the plastic deformation occurs as the film reaches its maximum flow stress [7]. Also over this range, partial phase transformations are possible [44].

The large relaxation of stress in the tensile direction at ~240 °C is the result of the transformation of the as-deposited β-Ta structure to the α-Ta structure. This is confirmed by XRD and resistivity results. β-Ta has a tetragonal crystal structure that transforms to α-Ta which has a bcc crystal structure. Two mechanisms that explain the change in stress are densification and grain growth. Calculations of change in stress based on β and α densities and grain growth can confirm this. Using reported phase densities of ρ_α = 16.65 g/cm^3 and ρ_β = 16.33 g/cm^3 [59] [60], the elastic constants can be approximated as the simple isotropic polycrystalline average (E=185 GPa, ν=0.28) [44]. Then a derivation done by Thompson and Carel can be utilized to acquire stress changes for both densification and grain growth [61].

$$\Delta\sigma_{densification} = -\frac{E}{1-\nu}\left(\frac{\rho_\alpha - \rho_\beta}{3\rho_\alpha}\right)$$

Using the previously stated values for E, ν, and the densities, a change in stress of 1.64 GPa is calculated. This accounts for the film transforming entirely from β to α phase.

The second consideration for stress changes is grain growth and its effect on excess volume. Using the Scherrer analysis, the grain size of our as-deposited and annealed films was determined [62]. The calculated values for the as-deposited and annealed grain sizes are d_0 = 35 nm and d_1 = 83 nm, respectively.

$$\Delta\sigma_{grain\ growth} = -\frac{E}{1-\nu}\,\delta\left(\frac{1}{d_1} - \frac{1}{d_0}\right)$$

Using the previously stated values for E, ν, and grain sizes and where the average excess volume per unit area $\delta = 1$ Å, a change in stress of 0.42 GPa is calculated.

The combined maximum change in stress predicts about a 2 GPa shift. Based on the stress relaxation in Figure 31 (a), the change is stress is approximately 1.7 GPa. Because of the estimations made in the calculations and variation in the data, these the predicted and experimental values roughly associate.

Reported transformation temperatures for Ta thin films has varied from 300-800 °C [7] [32] [44] [63] [64]. An important consideration here is the oxygen content of the system; either on the substrate surface or in the sputter gas [31]. In general, β-Ta forms on oxide substrates through a TaO_2 template layer [28] [29] [43]. Our as-deposited samples underwent no cleaning steps outside of a N_2 burst, meaning a native oxide was present upon deposition. Therefore, our expectations were to see β-Ta form. Another form of promoting β-Ta growth is the addition of oxygen to the sputter gas [31] [44]. Knepper *et al*. investigated the dependence of β-α transformation temperature on the oxygen partial pressure during deposition. They found higher oxygen partial pressures correlated with higher transformation temperatures [44]. With no additional oxygen gas added to the sputter gas during our depositions, a transformation temperature of 240 °C was achieved.

The lower phase transformation temperature than previously reported could be due to a lower amount of impurities in the system. The results for the post-system cleaning RGA in Figure 8, show no contaminant's partial pressures reaching above $5x10^{-8}$ Torr. Impurities introduced to the film surface have been shown to delay phase transformation [8] [43] [44] [58].

The stress relaxation during phase transformation is not complete, remaining with -0.5 GPa of compressive stress. Previous studies have shown incomplete transformations to result in partial

stress relaxation [44]; however, since the initial transformation temperature is exceeded by 100 °C this is not the case.

At the maximum temperature of the anneal, again there is a large change in stress from -0.5 – 2.25 GPa. This is a result of the experimental setup and not a phase transformation. Other sources have reported increases in compressive stress following the β-α phase transformation; however, each instance the sample follows thermoelastic behavior [7] [44]. In our case, the samples are exposed to the heating lamps turning off and on in succession. This results in thermal gradients developing across the thickness of the samples. This causes significant changes in substrate curvature due to thermal expansion of either surface.

In conclusion, despite the limits of the experimental setup, the annealing of as-deposited β-Ta produces a phase transformation to α-Ta. Resistivity and XRD results confirm this, but similar literature studies also report comparable thermal cycles. The transformation temperature is lower than previously reported at 240 °C and this is due to the low oxygen content in our UHV system. Heated deposition consistently resulted in α-Ta as confirmed by resistivity and XRD results. The pre-heating effects the initial deposition of Ta by evaporating oxygen and H_2O or other hydroxyl groups. The continued heating during deposition did not affect the film thickness and lowered the intrinsic compressive stress of the film.

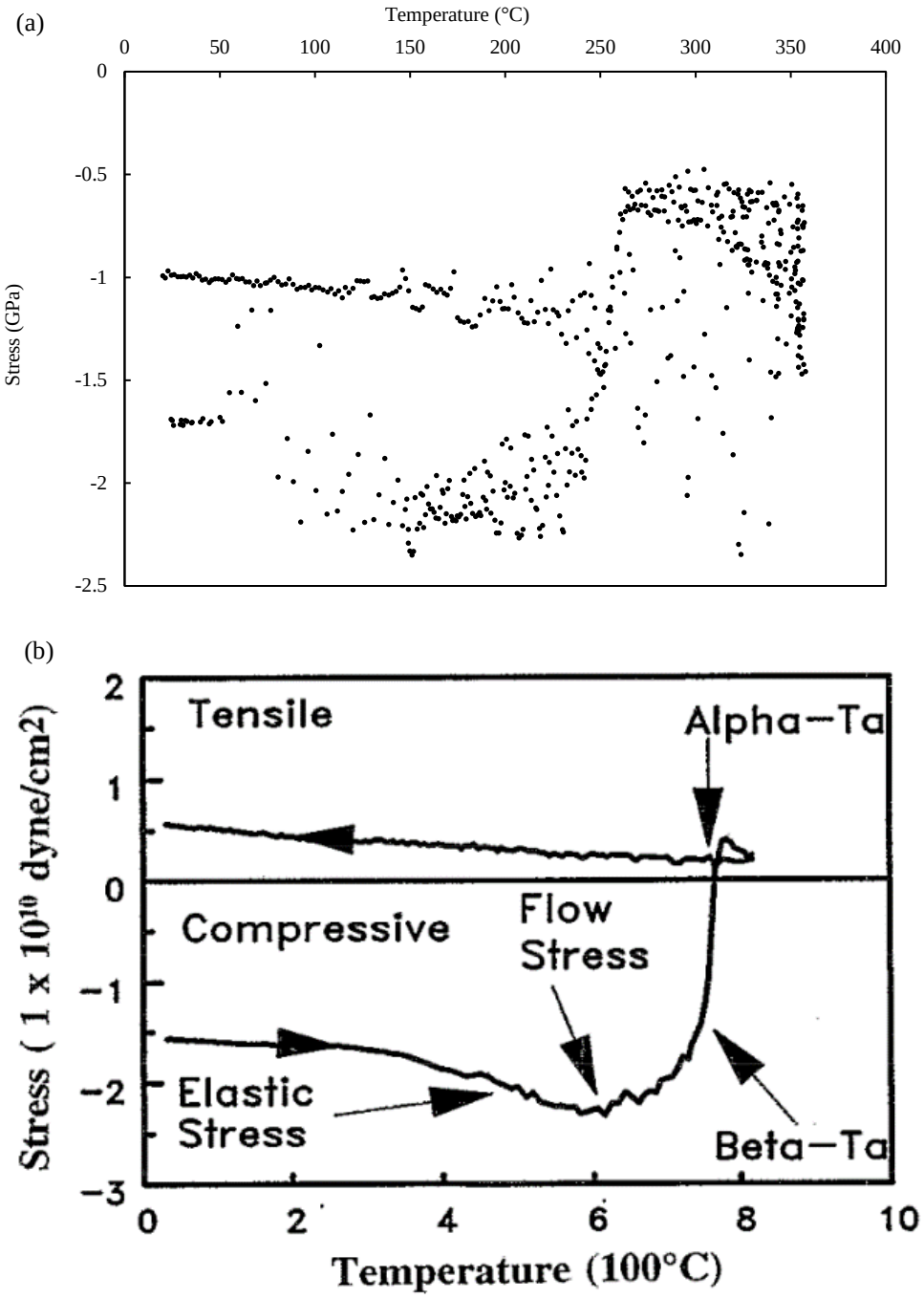

Figure 31: (a) Biaxial in-plane stress versus temperature of the sample for Ta thin films during annealing. (b) Stress versus temperature for Ta thin film during annealing [7]. Reproduced from [http://dx.doi.org/10.1063/1.352059], with the permission of AIP Publishing.

4.2 PHASE IDENTIFICATION AND SELECTION

Asymmetric PXRD was performed on as-deposited and heat-treated samples to determine the phase of the Ta thin film and its crystalline structure. In 1965, the crystal structure of β-Ta was determined to be tetragonal [1]. Following this discovery in 1972, Moseley and Seabrook's powder XRD results suggested that β-Ta is a Frank-Kasper σ structure with the $P4_2/mnm$ space group based on lattice parameter calculations from the (002) texture [22] [65]. In 2002, Arakcheeva *et al.* synthesized single crystal β-Ta and through diffraction experiments found a distorted Frank-Kasper σ structure. As a result, Arakcheeva et al. proposed that β-Ta has a $P\bar{4}2_1m$ space group [23]. The distinguishing feature of the distorted σ structure are the (001) and (003) diffraction peaks. Other literature sources have since identified (001) and (003) peaks in β-Ta, substantiating Arakcheeva's result [43] [60] [66] [67] [68].

Figure 32 shows the diffraction pattern of as-deposited Ta, revealing a textured thin film. The (002) and (004) β-Ta diffraction peaks are identified at 39.5° and 84.8°, respectively [53]. The (003) peak is not visible, hinting at the originally proposed $P4_2/mnm$ space group. However, a longer scan time for greater resolution should be utilized to confirm or deny this observation. Additionally, it is possible α-Ta diffraction peaks (110) and (211) are visible at 45.1° and 83.3°, respectively. This suggests a partial phase transformation has occurred resulting in α-Ta being present. Another consideration is that the substrate (400) Si peak at 82.4° is overlapping with the nearby diffraction peaks.

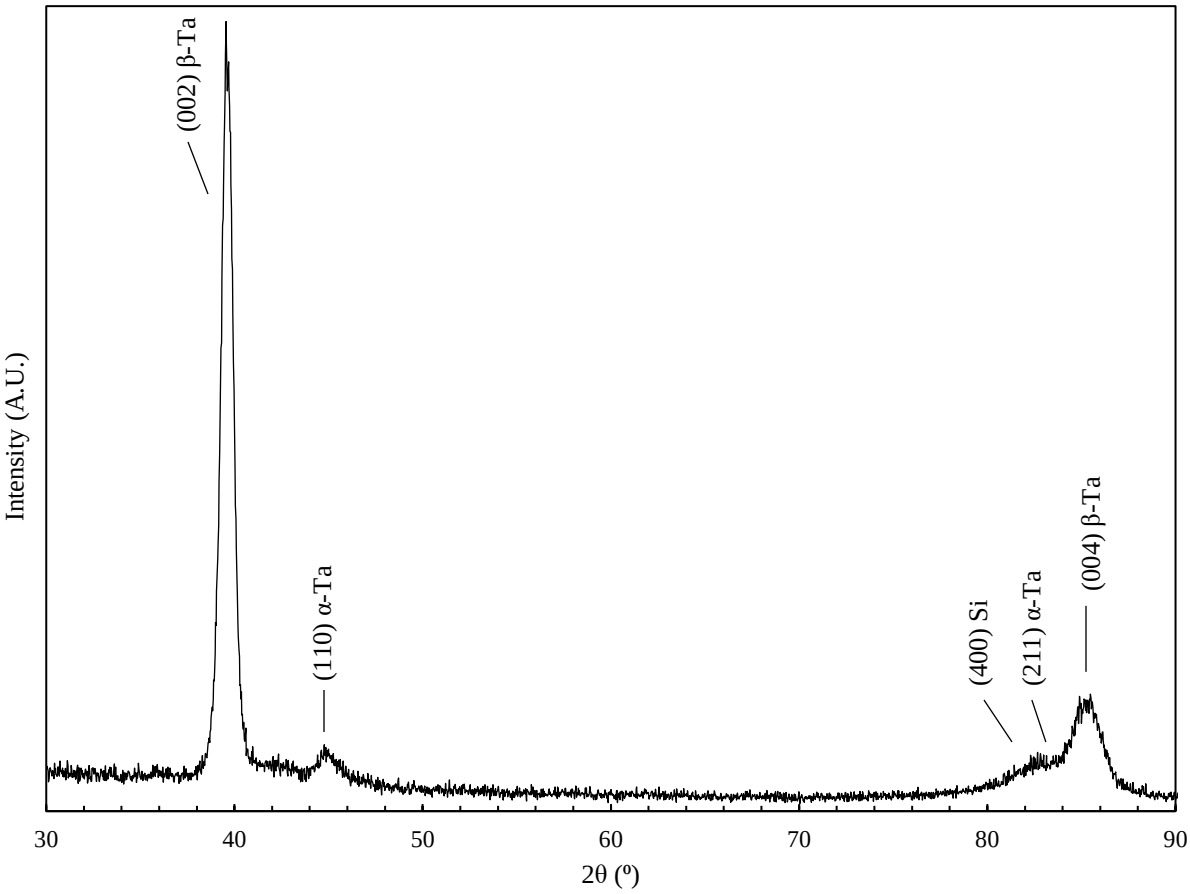

Figure 32: Asymmetric PXRD symmetric ω-2θ scans of an as-deposited Ta thin film.

Figure 33 shows the diffraction pattern of heated deposition Ta, revealed multiple textures in the thin film but with a preferred orientation of (110). The (110), (200), and (211) α-Ta diffraction peaks are identified at 45.1°, 65.7°, and 83.3°, respectively [51] [52]. In addition, the (102) TaS_2 diffraction peak is seen at 40.9°. No β-Ta peaks are seen suggesting that $TaSi_2$ formed at the interface followed by α-Ta during deposition.

The result of β-Ta formation for as-deposited Ta thin film supports the idea that oxygen impurities form TaO_2 which promote β-Ta [31] [43] [45]. Without any prior cleaning, samples are likely to have a native SiO_2 layer which could oxidize Ta. The result of α-phase formation for annealed and heated deposition thin films supports the idea that preheating and thermal activation

promote α-Ta [28] [31] [32]. The evaporation of absorbed water, removing a source of oxygen, as well as diffusion of Ta and Si removes oxide layers and promotes a $TaSi_2$ layer [46].

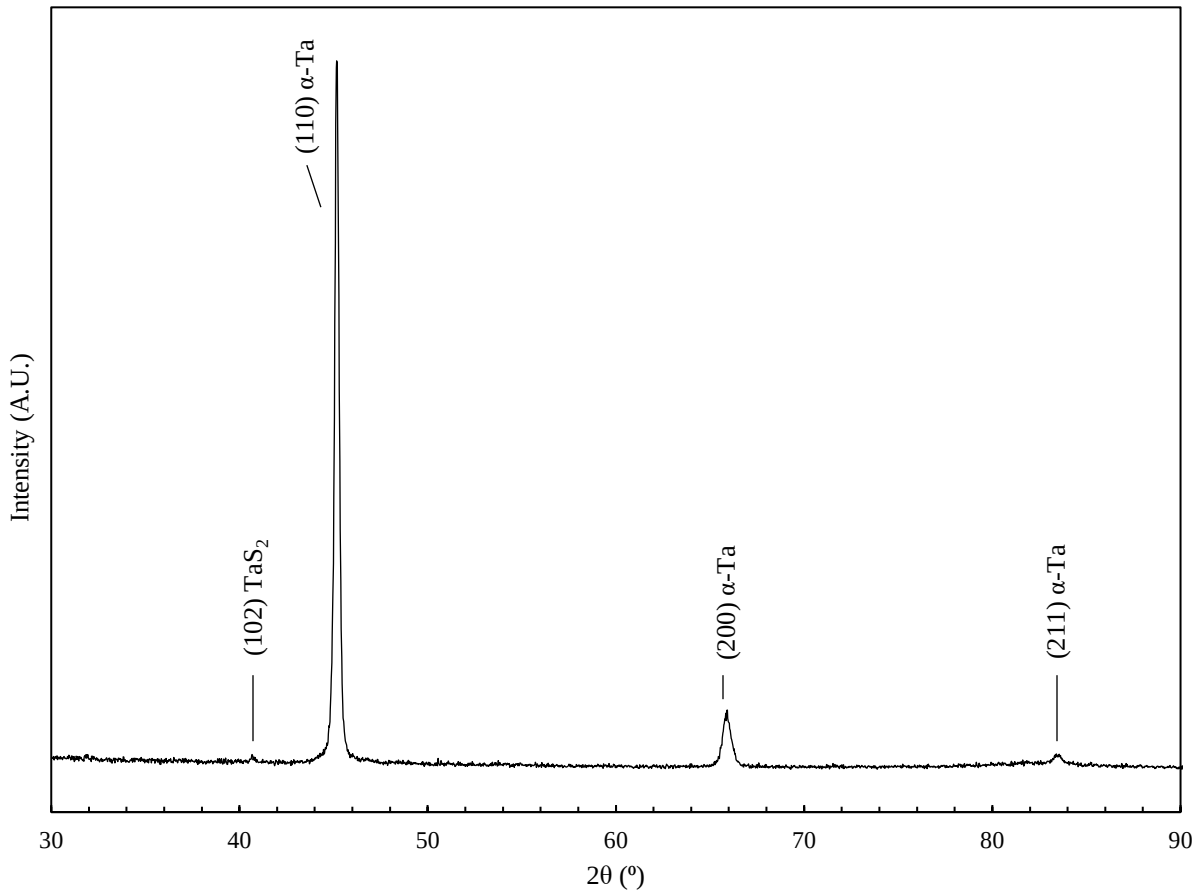

Figure 33: Asymmetric PXRD symmetric ω-2θ scans of a heated deposition Ta thin film.

In conclusion, XRD measurements of the as-deposited sample show primarily the (002) β-Ta diffraction peak. Like other studies of the β-phase, (002) is the main texture; however, the $P4_2/mnm$ or $P\bar{4}2_1m$ space group cannot be confirmed. XRD measurements of the annealed and heated deposition samples show the (110) α-Ta diffraction peak as well as the other cubic reflections. In addition, there is a low intensity (102) $TaSi_2$ diffraction peak.

4.3 X-RAY PHOTOELECTRON SPECTROSCOPY

XPS was performed to verify the film thickness and study the formation of tantalum silicide at the substrate/film interface. Figure 34 is a close examination of the Si 2p binding energy peak for the as-deposited, annealed, and heated deposition samples. The result gathered from Figure 34 (a) is that our as-deposited samples are approximately 250 nm thick. This somewhat agrees with previous findings in our lab which estimated the film thickness to be 200 nm based on the specific deposition conditions [49]. Figure 34 (b) and (c) show the Si 2p peak appearing earlier, around 210 nm into the sample. These samples underwent heat treatments but were deposited under the same sputtering conditions. This suggests diffusion at the Ta/Si interface, generating tantalum silicide. Zier *et al.* performed an investigation of ultra-thin film Ta on Si and observed a peak shift in the Si 2p binding energy. Using target factor analysis, it was proposed that the $TaSi_2$ present effects the bulk-Si 2p peak [69]. Similarly, a 1.4 eV shift from the bulk-Si 2p peak of 100.4 eV to 99 eV was observed throughout the samples. Combined with the $TaSi_2$ diffraction peaks in the GIXRD results, this confirms the presence of $TaSi_2$ in the samples.

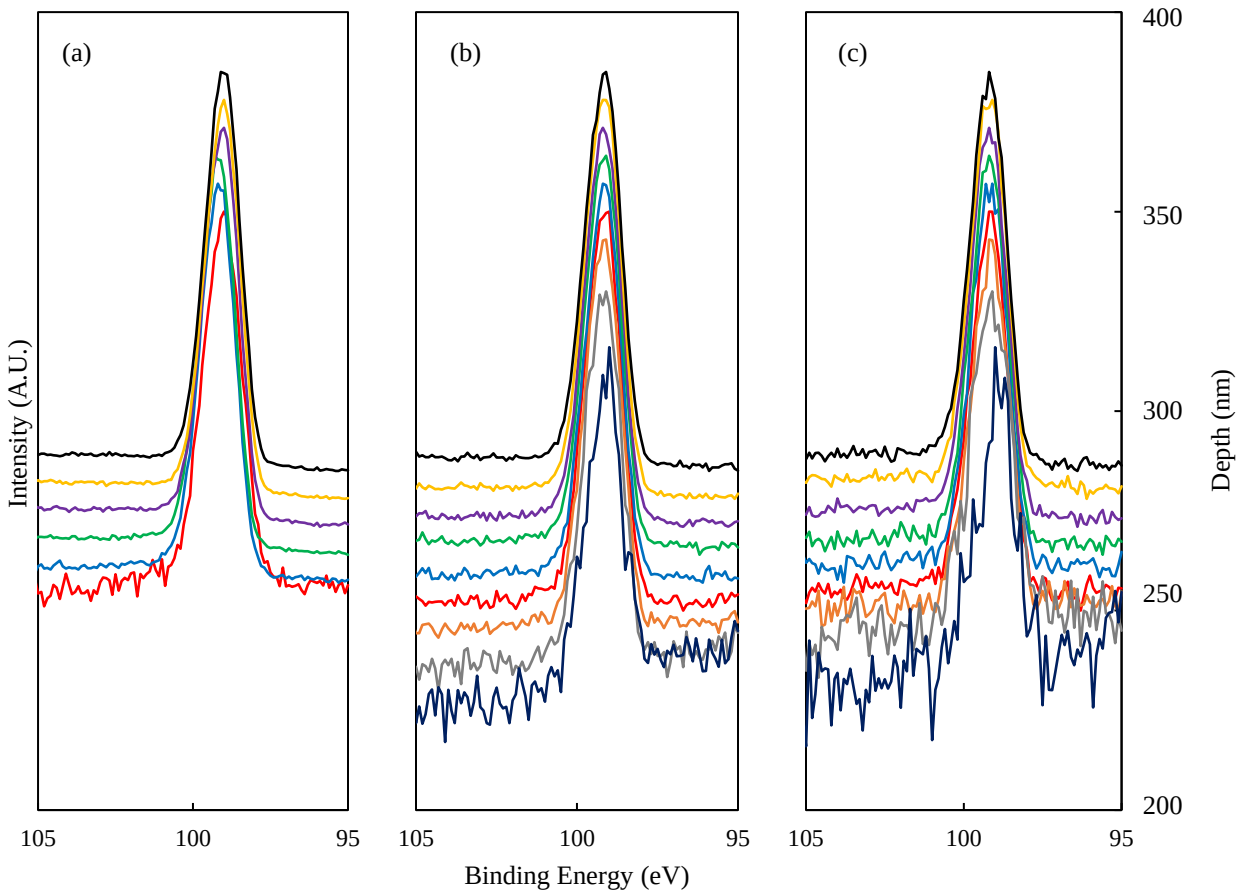

Figure 34: An XPS scan of the Si 2p electron configuration displaying intensity versus binding energy for as-deposited (a), annealed (b), and heated deposition (c) Ta thin film samples. The depth of the XPS scan is also displayed.

Figure 35, Figure 37, and Figure 37 are comparisons of the Ta 4f peak at different depths for the as-deposited, annealed, and heated deposition, respectively. Similar to the peak shift seen in the Si 2p peak, the Ta 4f peak also undergoes a shift when at the Ta/Si interface [69]. In Figure 35, the top layer (a) is the surface of the film which has been exposed to oxygen. Here Ta_2O_5 XPS peaks are present as expected. The interior layers (b) of the film match the bulk Ta 4f binding energy peak of 21.6 eV [54]. At the Ta/Si interface (c), there is a peak shift of 0.5 eV. This shift occurs at the same depth at which Si 2p peaks appear. In Figure 36, representing the annealed sample, similar layers appear initially. The surface (a) has Ta_2O_5 peaks, followed by the interior of

the film (b) matching bulk Ta 4f peaks. The Ta/Si interface at a lower depth (~200 nm) and the corresponding peak shift is more gradual. The resulting peak shift is less, 0.1 eV at the maximum depth. This indicates a $TaSi_2$ region as diffusion of Si and Ta occurs more readily under heated conditions. In Figure 37, representing the heated deposition sample, the layers are nearly identical when compared to the annealed sample. The resulting peak shift is approximately the same, 0.1 eV at the maximum depth. From this analysis, it is evident that the annealed and heated treated samples have thicker Ta-Si interface regions in which $TaSi_2$ has formed.

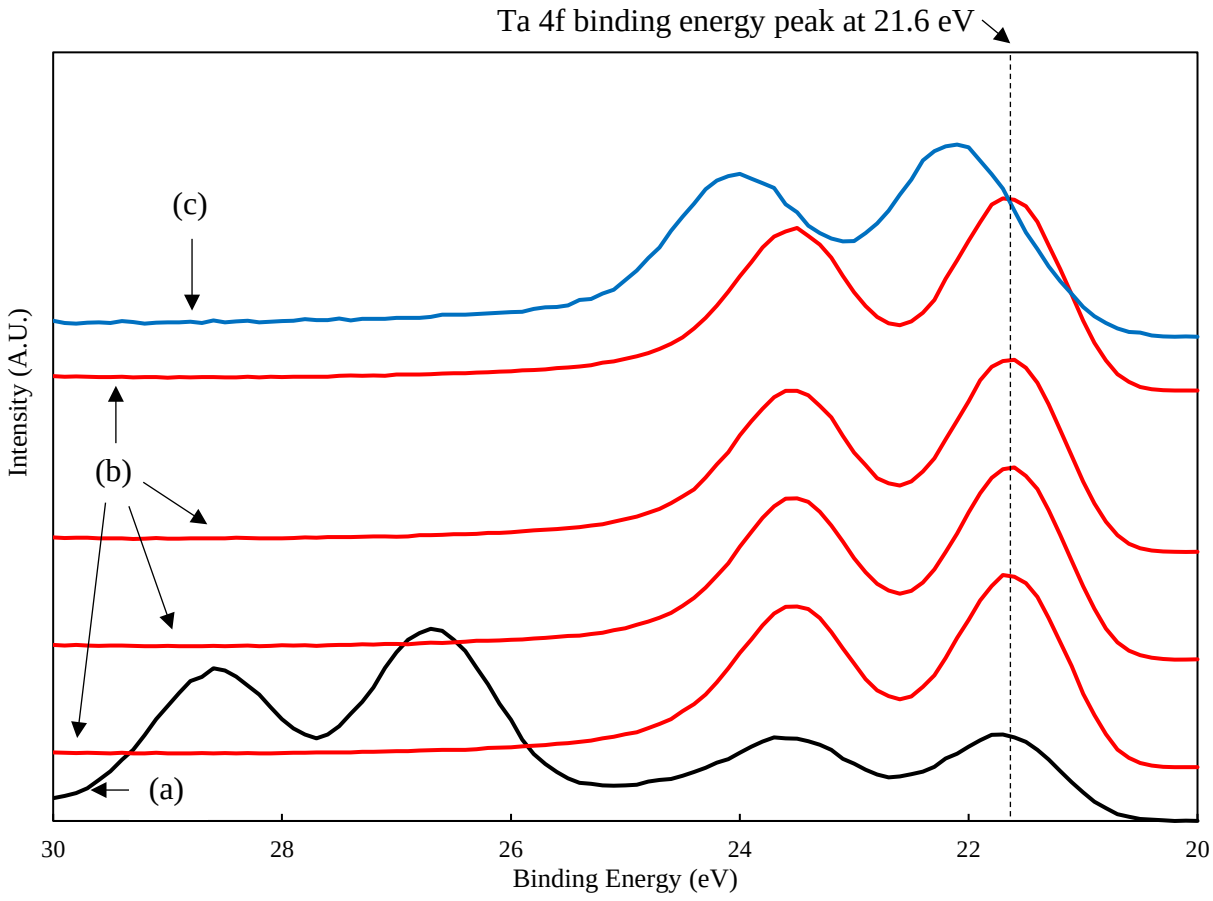

Figure 35: A comparison of XPS scans at different depths of the Ta 4f peak for the as-deposited samples. (a) The Ta thin film surface, exposed to oxygen. (b) The Ta thin film interior. (c) The Ta/Si interface.

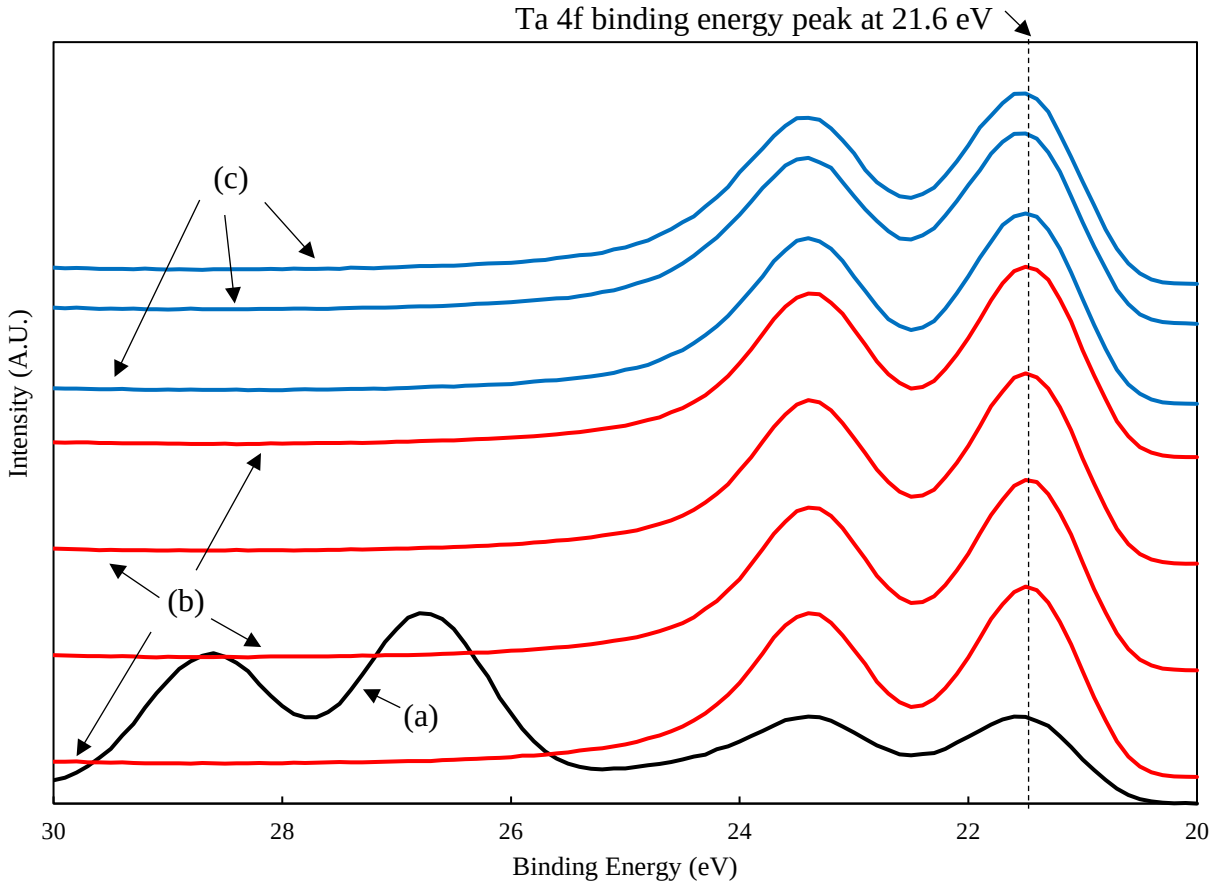

Figure 36: A comparison of XPS scans at different depths of the Ta 4f peak for the annealed samples. (a) The Ta thin film surface, exposed to oxygen. (b) The Ta thin film interior. (c) The Ta/Si interface.

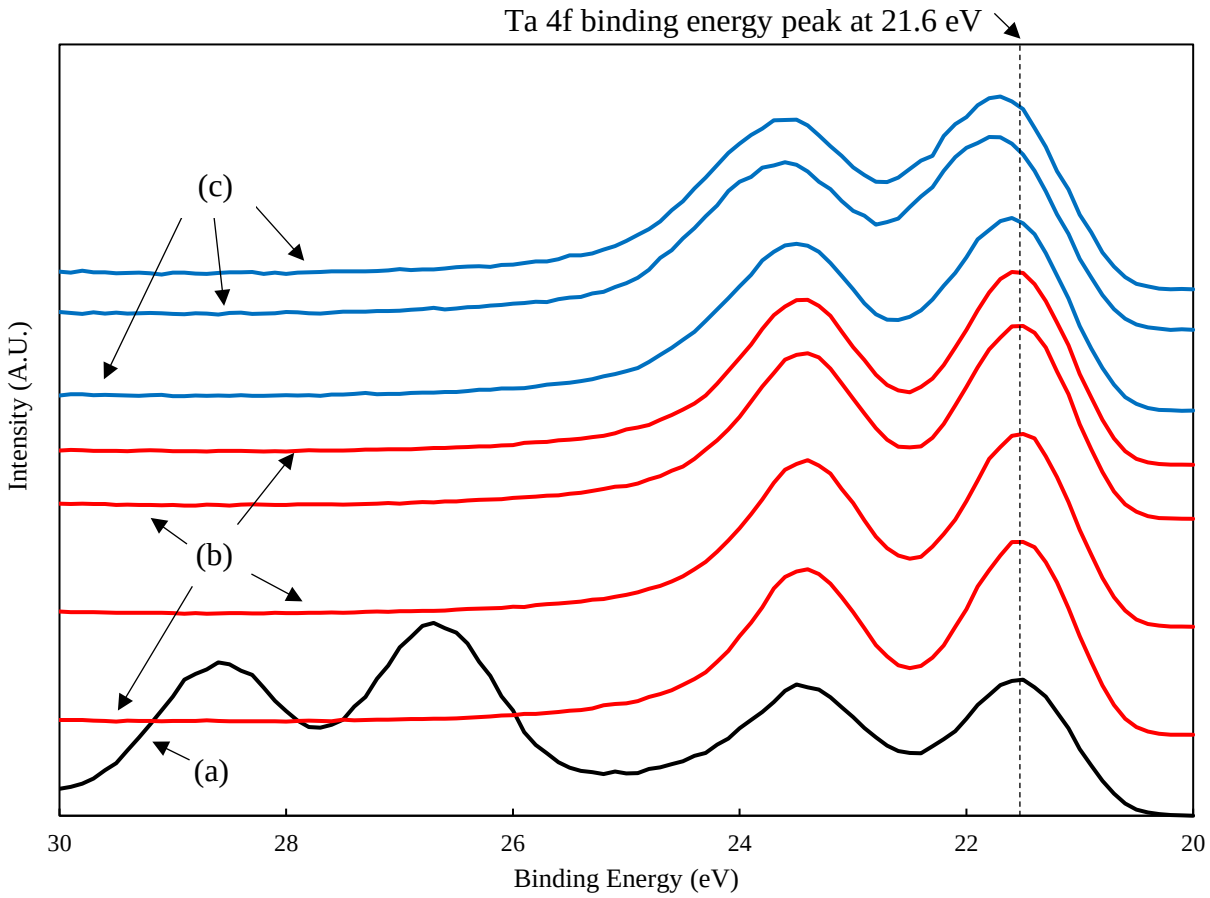

Figure 37: A comparison of XPS scans at different depths of the Ta 4f peak for the heated deposition samples. (a) The Ta thin film surface, exposed to oxygen. (b) The Ta thin film interior. (c) The Ta/Si interface.

XPS measurements in conjunction with ion milling found that the film thickness deposited was 250 nm. Peak shifts in the Ta 4f and Si 2p binding energies along with the earlier appearance of Si peaks indicate the presence of a $TaSi_2$ layer in annealed and heated deposition samples. The annealed and heated deposition samples XPS scans were comparable, meaning there are no differences in film thickness or composition. In addition, no oxygen or argon binding energy peaks were found, disregarding the surface scan. This indicates films free of those impurities.

5.0 CONCLUSION

An initial goal was set to engineer an experimental setup capable of generating α-phase Ta thin films. A new substrate holder was designed to allow for *in-situ* stress evolution measurements during deposition and annealing. The maximum temperature experienced by the substrate was improved to 350 °C. Ta thin films were successfully deposited via UHV magnetron sputtering.

The purpose of characterizing these samples was to identify the Ta phases present and identify the mechanisms by which they appear.

- During annealing, a β to α phase transformation was observed at 240 °C. This value is lower than previously reported transformation temperatures, as others hypothesized impurities can delay phase transformation. The low amount of impurities in our closed, small chamber system contributed to lowering the transformation temperature.
- Stress evolution measurements during deposition observe ~2 GPa of compressive stress. This value agrees with studies on low sputter pressure effects on film stress. During heated deposition, a lower compressive stress was observed while producing a similar thickness α-Ta film.
- Pure α-Ta was produced by pre-heating and heated deposition. This was due to improved gas and substrate surface purity.
- XPS measurements found the annealed and heated deposition samples to have a thicker Ta-Si interface than the as-deposited sample. XPS and XRD results revealed the presence of $TaSi_2$ in these heated samples.

6.0 FUTURE WORK

In this project, the influence of annealing and heated deposition on the phase and texture of Ta thin films was studied. A major limitation in the experimental setup was the method of heating the sample. Significant improvements could be made in avoiding or improving the fluctuating quartz heat lamp intensities. The substrate holder design could be reconsidered or a better method of operating the heat controller could be established. Attempts had been made to create a PC to heat controller communications possible but failed. Lastly, more accurate thermal calibrations could be made.

In future work, repeated annealing at different heating rates could reveal more regarding the thin film's behavior. Heated depositions could be performed at various temperatures.

In future work as far as characterization steps, rocking curves with the XRD would open discussion about the texture of various thin films. Also, EBSD could accomplish this by viewing the crystal orientation at the surface of the film. Additionally, how oxygen forms tantalum oxide and what structure promotes β-Ta could be an area of study.

BIBLIOGRAPHY

[1] M. Read and C. Altman, "A new structure in tantalum thin fillms," *Appl. Phys. Lett.*, 1965.

[2] J. F. Papp, "2010 Minerals Yearbook," *Department of the Interior, U.S. Geological Survey*, pp. 52.1-52.14, 2010.

[3] J. Zhang, Y. Huai, L. Chen and J. Zhang, "Formation of low resistivity alpha Ta by ion beam sputtering," *J. Vac. Sci. Technol. B Microelectron. Nanom. Struct.*, vol. 21, p. 237, 2003.

[4] M. Shiojiri, S. Shinkai, K. Sasaki, H. Yanagisawa and Y. Abe, "Preparation of low-resistivity alpha-Ta thin film on (001) Si by conventional DC magnetron sputtering," *Jpn. J. Appl. Phys.*, vol. 42, pp. 4499-4500, 2003.

[5] P. M. T. S. F. Sajovec, "Structural and electrical properties of ion beam sputter deposited tantalum," *Thin Solid Films*, vol. 219, pp. 206-209, 1992.

[6] N. Schwartz, W. Reed and P. Polash, "Temperature coefficient of resistance of beta-tantalum films and mixtures with b.c.c.-tantalum," *Thin Solid Films*, vol. 14, pp. 333-347, 1972.

[7] L. Clevenger, A. Mutscheller, J. Harper, C. Cabral and K. Barmak, "The relationship between deposition conditions, the beta to alpha phase transformation, and stress relaxation in tantalum thin films," *Journal of Applied Physics*, vol. 72, no. 10, 1992.

[8] A. Navid and A. Hodge, "Controllable residual stresses in sputtered nanostructured alpha-tantalum," *Scr. Mater.*, vol. 63, pp. 867-870, 2010.

[9] Y. Zhou, Z. Xie, H. Xiao, P. Hu and J. He, "Effects of deposition parameters on tantalum films deposited by direct current magnetron sputtering in Ar-o2 mixture," *Appl. Surf. Sci.*, vol. 83, pp. 286-291, 2008.

[10] G. Chen, P. Lee and S. Che, "Phase formation behavior and diffusion barrier property of reactively sputtered tantalum-based thin films used in semicionductor metallization," *Thin Soild Films,* vol. 353, pp. 264-273, 1999.

[11] F. L. W.D. Westwood, " Phase composition and conductivity of sputtered tantalum," *Thin Solid Films ,* 1970.

[12] L. B. Freund and S. Suresh, Thin Film Materials: Stress, Defect Formation and Surface Evolution, Cambridge University Press, 2009.

[13] M. Ohring, Materials Science of Thin Films - Deposition and Structure, Elsevier, 2002.

[14] D. Depla, Reactive Sputter Deposition, New York: Springer, 2008.

[15] P. Catania, R. A. Roy and J. J. Cuomo, "Phase formation and microstructure changes in tantalum thin films induced by bias sputtering," *J. Appl. Phys.,* vol. 74, pp. 1008-1014, 1993.

[16] C. Aita, "Glow discharge mass spectrometry of sputtered tantalum nitride," *J. Vac. Sci. Technol.,* vol. 18, p. 324, 1981.

[17] M. Grosser and U. Schmid, "The impact of sputter conditions on the microstructure and on the resistivity of tantalum thin films," *Thin Solid Films ,* vol. 517, pp. 4493-4496, 2009.

[18] D. Face, "Nucleation of body-centered-cubic tantalum films with a thin niobium underlayer,," *J. Vac. Sci. Technol. A Vacuum, Surfaces, Film 5,* p. 3408, 1987.

[19] C. V. Thompson, "Structure Evolution During Processing of Polycrystalline Films," *Annual Review of Materials Science ,* vol. 30, pp. 159-190, 2000.

[20] E. Chason, "Resolution and sensitivity of stress measurements with the k-Space Multi-beam Optical Sensor (MOS) System," k-Space Associates, 2018.

[21] G. Stoney, "The Tension of Metallic Films Deposited by Electrolysis," *Proc. R. Soc. London,* vol. Ser. A, no. 82, pp. 172-175, 1909.

[22] P. Moseley and C. Seabrook, "The crystal structure of beta-tantalum," *Acta Cryst.,* vol. 29, pp. 1170-1171, 1973.

[23] A. Arakcheeva, G. Chapuis and V. Grinevitch, "The self-hosting structure of β-Ta," *Acta Cryst.,* vol. 58, pp. 1-7, 2002.

[24] J. Senkevich, T. Karabacak, D. Bae and T. Cale, "Formation of body-centered-cubic tantalum via sputtering on low-k dielectrics at low temperatures," *J. Vac. Sci. Technol. B Microelectron. Nanom. Struct,* vol. 24, p. 534, 2006.

[25] S. Lee, M. Doxbeck, J. Mueller, M. Cipollo and P. Cote, "Texture, structure and phase transformation in sputter beta tantalum coating," *Surf. Coating. Technol.,* vol. 177, pp. 44-51, 2004.

[26] L. Kotis, M. Menyhard, A. Sulyok, G. Safran, A. Zalar, J. Kovac and P. Panjan, "Determination of the relative sputtering yield of carbon to tantalum by means of Auger electron spectroscopy depth profiling," *Surf. Interface Anal. ,* vol. 41, pp. 799-803, 2009.

[27] L. Liu, C. Pai, H. Tseng, D.C. and R. Buhrman, "Spin-torque switching with the giant spin Hall effect of tantalum," *Science,* vol. 336, 2012.

[28] L. Feinstein and R. Huttemann, "Factors controlling the structure of sputtered Ta films," *Thin Solid Films,* vol. 16, no. 2, pp. 129-145, 1973.

[29] S. Shigehiko, "Nucleation properties of magnetron-sputtered tantalum," *Thin Solid Films,* vol. 94, no. 4, pp. 321-329, 1982.

[30] T. Tyson and A. Jiang, "The structure and stability of beta-Ta thin films," *Thin Solid FIlms,* vol. 479, pp. 166-173, 2005.

[31] A. Schauer and M. Roschy, "R.F. sputtered β-tantalum and b.c.c. tantalum films," *Thin Solid Films,* vol. 12, no. 2, pp. 313-317, 1972.

[32] C. Whitman, "Effect of various sputtering parameters on Ta phase formation using an I-Optimal experimental design," *J. Vac. Sci. Technol. B Microelectron. Nanom. Struct.,* vol. 18, 2000.

[33] W. P. G. R. J. Sosniak, "Effect of background-gas impurities on the formation of sputtered beta-tantalum films," *J. Appl. Phys. ,* 1967.

[34] H. Ren and M. Sosnowski, "Tantalum thin films deposited by ion assisted magnetron sputtering," *Thin Solid Films,* vol. 516, pp. 1898-1905, 2008.

[35] K. Ino and T. Shinohara, "Ion energy , ion flux , and ion species effects on crystallographic and electrical properties of sputter-deposited Ta thin films," *J. Vac. Sci. Technol.,* vol. A, no. 15, pp. 2627-2635, 1997.

[36] R. Roy, " Role of energetic atoms and ions in Ta films grown by different physical vapor deposition methods," *J. Vac. Sci. B. Morcoelectron. Nanom. Struct.,* vol. 11, p. 1921, 1993.

[37] K. Valleti, A. Subrahmanyam and S. V. Joshi, "Growth of nano crystalline near α phase thin films at room temperature using cylindrical magnetron cathode," *Surf. Coatings Technol.*, vol. 202, pp. 3325-3332, 2008.

[38] R. Bradley, J. Harper and D. Smith, " Theory of thin-film orientation by ion bombardment during deposition," *J. Appl. Phys.*, vol. 60, pp. 4160-4164, 1986.

[39] G. V. Wyk and H. Smith, "Crystalline reorientation due to ion bombardment," *Nucl. Instrum. Meth.* , vol. 170, pp. 433-439, 1980.

[40] L. Gladczuk, A. Patel, C. Paur and M. Sosnowski, "Tantalum films for protective coatings of steel," *Thin Solid Films,* vol. 467, pp. 150-157, 2004.

[41] L. Gladczuk, A. Patel, J. Demaree and M. Sosnowski, "Sputter deposition of bcc tantalum films with TaN underlayers for protection of steel," *Thin Solid Films,* vol. 476, pp. 295-302, 2005.

[42] J. Thornton, " Substrate heating in cylindrical magnetron sputtering sources," *Thin Solid Films,* vol. 54, pp. 23-31, 1978.

[43] E. Ellis, M. Chmielus and S. Baker, "Effect of sputter pressure on Ta thin films: Beta phase formation, texture, and stresses," *Acta Materialia,* vol. 150, pp. 317-326, 2018.

[44] R. Knepper, B. Stevens and S. Baker, "Effect of oxygen on the thermomechanical behavior of tantalum thin films during the β–α phase transformation," *Journal of Applied Physics,* vol. 100, 2006.

[45] N. Waterhouse, P. Wilcox and D. Willmott, "Effect of oxygen on the electrical and structural properties of triode-sputtered tantalum films," *J. Appl. Phys.*, vol. 42, p. 5649, 1971.

[46] W. Westwood, D. Willmott and P. Wilcox, "Tantalum films triode-sputtered in mixtures of argon and water vapor," *J. Vac. Sci. Technol.*, vol. 9, p. 987, 1972.

[47] Extorr, "Instruction Manual Extorr XT Series RGA," Extorr Inc., New Kensington.

[48] S. Getters, "CapaciTorr Pumps MK5 Series - General Information," SAES Getters Group, 2001.

[49] E. Sullivan, "Influenece of sputter power and wafer plasma cleaning on stress and phase formation of as-deposited tantalum thin films," University of Pittsburgh, MEMS 1079: Senior Research, 2015.

[50] Jandel, "Microposition Probe," Jandel Engineering Ltd., Linslade, 2003.

[51] M. Mueller, *Scripta Metallurgica,* vol. 11, p. 693, 1977.

[52] M. Ohtani and Y. K. W. Hirata, *High Temperatures-High Pressures,* vol. 7, p. 221, 1975.

[53] V. V. Grinevich, P. Pattison, H. Birkedal, G. Chapuis and A. Arakcheeva, *Acta Crystallographica B,* vol. 59, no. 324, 2003.

[54] B. V. Crist, Handbooks of Monochromatic XPS Spectra - The Elements and Native Oxides, XPS International, Inc, 1999.

[55] J. Thornton and D. Hoffman, "Internal stresses in titanium, nickel, molybdenum, and tantalum films deposited by cylindrical magnetron sputtering," *J. Vac. Sci. Technol.,* vol. 14, pp. 164-169, 1977.

[56] E. Chason, "A kinetic analysis of residual stress evolution in polycrystalline thin films," *Thin Solid Films,* vol. 526, pp. 1-14, 2012.

[57] F. D'Heurle, L. Berenbaum and R. Rosenberg, *Trans. Met. Soc. AIME,* vol. 242, no. 502, 1968.

[58] N. Schwartz and E. D. Feit, "Impurity Effects in the Nucleation of Alpha (bcc)-Tantalum or Beta-Tantalum Films," *J. Electrochem. Soc.,* vol. 124, no. 1, pp. 123-131, 1977.

[59] L. C. Feldman and J. W. Mayer, Fundamentals of Surface and Thin Film Analysis, Upper Saddle, NJ: Prentice-Hall, 1986.

[60] A. Jiang, A. Yohannan, N. O. Nolim, T. A. Tyson, L. Ax, S. L. L. and P. C. S. Films, *Thin Solid Films,* vol. 437, no. 116, 2003.

[61] C. V. Thompson and R. Carel, "Stress and grain growth in thin films," *J. Mech. Phys. Solids,* vol. 44, no. 5, pp. 657-673, 1996.

[62] P. Scherrer, *Nachr. Ges. Wiss. Goettingen, Math.-Phys. Kl.,* vol. 2, no. 96, 1918.

[63] C. Cabral, L. Clevenger and R. Schad, "Repeated compressive stress increase with 400 °C thermal cycling in tantalum thin films due to increases in the oxygen content," *Journal of Vacuum Science & Technology,* vol. 12, no. 2818, 1994.

[64] R. Knepper and S. Baker, "Coefficient of thermal expansion and biaxial elastic modulus of β phase tanatlum thin films," *Applied Physics Letters,* vol. 90, no. 181908, 2007.

[65] F. Frank and J. Kasper, "Complex alloy structures regarded as sphere packings. II. Analysis and classification of representative structures," *Acta Crystallographica,* vol. 12, pp. 483-499, 1959.

[66] S. L. Lee, M. Doxbeck, J. Mueller, M. Cipollo and P. Cote, "Texture, structure and phase transformation in sputter beta tantalum coating," *Surface and Coatings Technology,* Vols. 177-178, pp. 44-51, 2004.

[67] D. Bernoulli, U. Müller, M. Schwarzenberger, R. Hauert and R. Spolenak, "Magnetron sputter deposited tantalum and tantalum nitride thin films: an analysis of phase, hardness and composition," *Thin Solid Films,* vol. 548, pp. 157-161, 2013.

[68] R. Saha and J. Barnard, " Effect of structure on the mechanical properties of Ta and Ta(N) thin films prepared by reactive DC magnetron sputtering," *J. Cryst. Growth,* vol. 174, pp. 495-500, 1997.

[69] M. Zier, S. Oswald, R. Reiche and K. Wetzig, "XPS investigations of thin tantalum films on a silicon surface," *Anal Bioanal Chem,* vol. 375, pp. 902-905, 2003.